University of Nevada, Reno

Evaluating Seasonal Deformation in the Vicinity of Active Fault Structures in Central California Using GPS Data

A thesis submitted in partial fulfillment of the requirements
for the degree of Master of Science in Geophysics

by

Meredith L. Kraner

Dr. Cornelis Kreemer/Thesis Advisor

August, 2017

THE GRADUATE SCHOOL

We recommend that the thesis
prepared under our supervision by

MEREDITH L. KRANER

Entitled

Evaluating Seasonal Deformation in the Vicinity of Active Fault Structures in Central California Using GPS Data

be accepted in partial fulfillment of the
requirements for the degree of

MASTER OF SCIENCE

Cornelis Kreemer, Ph.D., Advisor

William C. Hammond, Ph.D., Committee Member

Ilya Zaliapin, Ph.D., Graduate School Representative

David W. Zeh, Ph.D., Dean, Graduate School

August, 2017

Abstract

Central California is a tectonically active region in the Western United States, which encompasses segments of both the San Andreas and Calaveras Faults and centers around the town of Parkfield, California. Recently, statistical studies of microseismicity suggest that earthquake rates in this region can vary seasonally. Also, studies using data from modern GPS networks have revealed that crustal deformation can be influenced by seasonal and nontectonic factors, such as hydrological, temperature, and atmospheric loads. Here we analyze eight-years (2008 – 2016) of GPS data and build on this idea by developing a robust seasonal model of dilatational and shear strain in Central California.

Using an inversion, we model each GPS time series in our study region to derive seasonal horizontal displacements for each month of the year. These positions are detrended using robust MIDAS velocities, destepped using a Heavyside function, and demeaned to center the time series around zero. The stations we use are carefully chosen using a selection method which allows us to exclude stations located on unstable, heavily subsiding ground and include stations on sturdy bedrock. In building our seasonal strain model, we first filter these monthly seasonal horizontal displacements using a median-spatial filter technique called GPS Imaging to remove outliers and enhance the signal common to multiple stations. We then grid these seasonal horizontal filtered displacements and use them to model our dilatational and shear strain field for each month of the year.

We setup our model such that a large portion of the strain in the region is accommodated on or near the San Andreas and Calaveras Faults. We test this setup using two sets of synthetic data and explore how varying the a priori faulting constraints of the on and off-fault standard deviations in the strain tensor affects the output of the model. We

additionally extract strain time series for key regions along/near the San Andreas and Calaveras Faults.

We find that the most prevalent seasonal strain signal exists in the main creeping section along the San Andreas Fault in Central California. This region, which runs from Parkfield to Bitterwater Valley, shows peaks in contraction (negative dilatation) during the wet period (February/March) and peaks in extension (positive dilatation) during the dry period (August/September). The north transitional creeping section along the San Andreas Fault and the Calaveras Fault displays general similarities with the main creeping section trend. In sharp contrast, seasonality is virtually undetected in the locked section of the San Andreas Fault south of the town of Cholame. Additionally, the southern transitional creeping section shows two distinct patterns. For the most part this region, between Parkfield and Cholame, shows peaks in contraction during the wet period (February/March) and peaks in extension during the dry period (August/September), similar to the main creeping section. However, the segment of the southern transitional creeping section surrounding the town of Cholame opposes this trend with peaks in extension during the wet period and peaks in contraction during the dry period. We postulate several causes for this seasonal signal, which we plan to explore further in future work.

To my parents, for their constant support and guidance.

Acknowledgements

This project was made possible through a NASA Earth and Space Science Fellowship NNX16AN98H to M.L. Kraner and C. Kreemer, SCEC grant 16154 to A.A. Borsa and C. Kreemer, NSF grant 1252210 to G. Blewitt and W.C. Hammond, and tuition assistance provided by the University of Nevada, Reno College of Science. GPS data for this project was processed by the Nevada Geodetic Laboratory at UNR using RINEX files obtained from the Plate Boundary Observatory Network operated by UNAVCO, the Bay Area Regional Deformation Network (BARD) operated by UC Berkeley, the United States Geological Survey (USGS), Caltrans Regional Survey Network, the United States Coast Guard (USCG), the Federal Aviation Administration (FAA), and SmartNet North America. Mapped California groundwater basins were obtained from the California Department of Water Resources, earthquake data from the Northern California Earthquake Data Center (NCEDC), and fault data from the USGS Fault and Fold Database. Figures for this project were prepared using Generic Mapping Tools [*Wessel and Smith,* 1998; *Wessel et. al.,* 2013] and MATLAB®.

I am deeply grateful to numerous individuals who contributed their time and effort towards this work. First, I would like to thank my advisors Dr. Corné Kreemer and Dr. Bill Hammond for providing support and continuous guidance through my degree. In coming to UNR, they gave me a freedom to expand on a research project started as undergraduate with Dr. Bill Holt and Dr. Daniel Davis at Stony Brook University. This project was greatly improved by input from Dr. Adrian Borsa from Scripps Institution of Oceanography located at UC San Diego. In addition, Adrian has been a great mentor for me, providing constant encouragement and excellent advice. I would like to thank Dr. Ilya Zaliapin for

serving on my committee and providing statistical assistance. Lastly, I thank Dr. Geoff Blewitt for processing all of the GPS data for this study.

I extend sincere thanks to my fellow graduate students and all of the faculty and staff members of the UNR seismology lab for their continuous encouragement. I would especially like to thank Justine O., Christine R., Courtney B., Heather W., Michelle D., and Kelley S., for their friendship. Specifically, my officemate, Justine, joined the GPS lab at a time of need for me. Discouraged and too involved in my work, Justine provided me with a life outside the lab including (but not limited to) baking parties, weekend movie suggestions, as well as hiking and ski trips in Tahoe. My roommates Shannon K. and Katryn D. are thanked for keeping me sane outside the realm of the geology department. All new graduate students living in this crazy town called Reno, we consulted on the best restaurants and coffee shops in town as well as casual life advice.

Thank you all!!

Table of Contents

List of Tables

List of Figures

1

Introduction and Background

1.1 Overview

Traditionally, theories of earthquake failure have been rooted in the elastic rebound theory [Reid, *1910*], where the earth's crust is thought to deform slowly at a constant rate until failure. However, numerous studies prove that this model is a relatively simple explanation of earthquake initiation. They suggest that seismogenic and rupture behavior vary greatly based on geometrical organization [e.g. *Wesnousky,* 2006], bedrock geology [e.g. *Schmalzle et al.,* 2006; *Titus et al.,* 2011], and slip behavior/rate [e.g. *Harris and Segall,* 1987; *Argus and Gordon*, 2001; *McCaffrey* 2005]. More recently, studies using data from modern GPS networks, InSAR satellites, and seismic networks provide convincing evidence that crustal deformation can be time-dependent as well as nontectonic in origin. This can be due to elastic responses to water loads [e.g. *Amos et al.*, 2014; *Borsa et al.*, 2014; *Argus et al.,* 2014], snow loads [e.g. *Heki* 2001; 2003], temperature [e.g. *Prawirodirdjo et al.*, 2006; *Tsai,* 2011; *Ben-Zion and Allam*, 2013], tidal loads [e.g. *Métivier et al.,* 2009; *Delorey et. al.,* 2017], atmospheric loads [e.g. *vanDam et al.*, 1994], in addition to poroelastic effects [e.g. *Argus et al.,* 2005; *Ji and Herring,* 2012; *Chaussard et al.,* 2014]. Additionally, statistical studies have shown how micro-seismicity can significantly vary throughout set (monthly to yearly) periods of time [e.g. *Christiansen et al.,* 2007; *Dutilleul et al.,* 2015].

Currently, conventional seismic hazard models ignore time-variability and stick to the traditional ideology proposed by *Reid* [1910]. Here I attempt to robustly identify coherent seasonal, time-dependent and nontectonic signals in time series of GPS data in Central California (purple-dashed box, Figure 1) and correlate them spatially across major

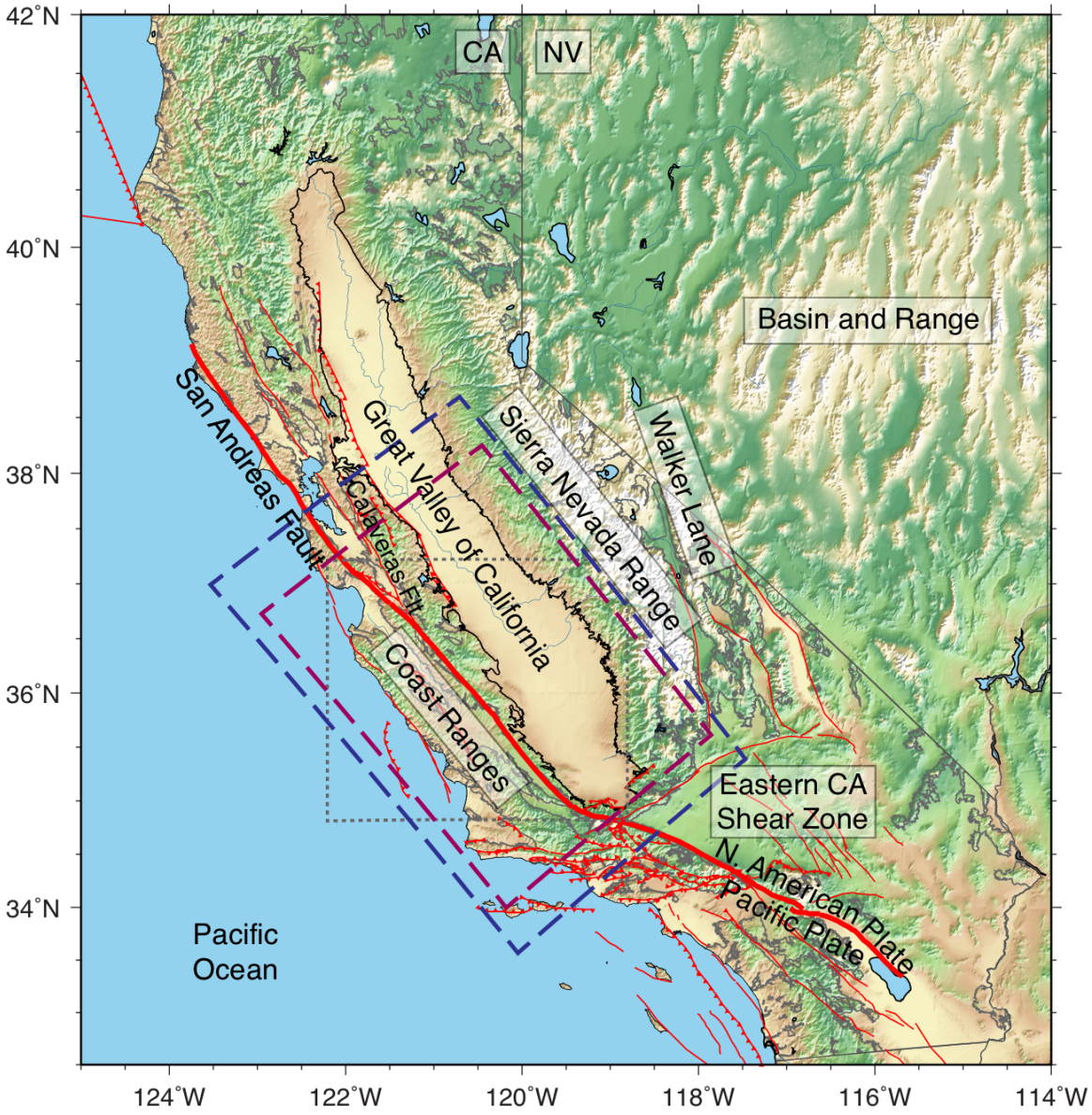

Figure 1 Central California study region in the Western United States. State borders of California (CA) and Nevada (NV) are outlined in gray. The blue-dashed outline designates the extent of input GPS data for this study and the purple-dashed outline is the analysis region plotted throughout this work. The gray dotted area is the boundary used for Figures A1 and A2 in the appendix. California faults from the USGS fault and fold database are drawn in red and basins are outlined in gray. The Great Valley of California is outlined in black.

fault structures through strain modeling in my study region. I select data from GPS stations lying on bedrock (rather than on unstable ground), and use the seasonal signals found at these stations to map patterns of seasonal displacement and strain across the San Andreas and Calaveras Faults in Central California. The results presented here suggest a correlation between seasonal (un-)loading of the creeping segment of the San Andreas Fault, seasonality, and water storage patterns. They also correlate with previous studies of seasonality in micro-seismicity patterns [e.g. *Christiansen et al.,* 2007].

1.2 Geologic Setting

Central California (purple-dashed box, Figure 1) is host to three major provinces: the Coast Ranges at the western extent of the study region, the Great Valley of California in the center, and the Sierra Nevada Range to the east of the study region (Figure 1). As described in the next section, this study region is tectonically active with its most active faulting structure, the San Andreas Fault, lying within the Coast Range region. Over the past 30 million years since the subduction of the Farallon Plate under the North America Plate [*Atwater,* 1970; *Atwater and Stock*, 1998; *Humphreys,* 2003], active strike slip displacement along the San Andreas Fault has worked to align two structurally/rheologically distinct regions into what is currently referred to as the Coast Ranges.

The San Andreas Fault marks the northeast extent of the Salinian block, which is mostly composed of granitic plutons and metamorphic rocks. This unit has been displaced northeast several hundred kilometers along the San Andreas Fault from its original location [*Page,* 1981; *Page et al.,* 1998]. Before its displacement, the ancestral margin of California

was an active subduction zone [*Blake and Jones*, 1981; *Dickinson,* 1981] mainly responsible for the formation of the terrain today located east of the San Andreas Fault. The Franciscan complex lies directly to the east of the San Andreas Fault and is thought to be the accretionary complex of the subducting Farallon Plate [*Blake and Jones,* 1981; *Dickinson,* 1981; *Page et al.,* 1998]. This is a sedimentary unit containing a mixture of oceanic mantle (serpentine) and crustal components (gabbros, basalts) in addition to sandstones, greywacke, and conglomerates [*Page et al.,* 1998]. Overlying the Franciscan complex is the Great Valley Sequence. It comprises of marine clastic shale and siltstone sediments with exposed remnants of the Coast Range ophiolite (bodies of serpentine) at the unit's base [*Irwin and Barnes*, 1975; *Page et al.,* 1998].

The Great Valley and Sierra Nevada Range, found to the east of the Great Valley Sequence/Franciscan Complex, are thought to (partially) be remnants of the forearc trough and magmatic arc (respectively) of this subduction event [*Blake and Jones,* 1981; *Dickinson,* 1981]. Over time, a large volume of sediments filled in the Great Valley structural trough, with thicknesses of up to 4 km within Central California study region [*Fliedner et al.*, 2000; *Faunt et al.,* 2009].

1.3 Tectonic Setting and Seismotectonics

Relative to a fixed Pacific Plate, the North American Plate migrates southwest at a rate of ~50 mm/year [*DeMets and Dixon*, 1999] and this deformation is distributed on faulting structures throughout the Western United States. The largest contributor to this motion is the well-developed, transpressional, northwest striking San Andreas Fault System [*Wesnousky,* 2005], which accommodates ~30 mm/yr of the Pacific-North American Plate Motion [*Savage and Burford*, 1973; *Lisowski and Prescott*, 1981; *Titus et*

al., 2005]. Smaller amounts of this relative plate motion are absorbed by the Walker Lane, Basin and Range, and Eastern California Shear Zone (Figure 1) [*Dixon et al.,* 2000; *Bennett et al.,* 2003; *Wesnousky,* 2005; *Kreemer et al.,* 2012].

Consequently, Central California lies within a seismogenically active region of the Western United States. Although several other structures exist in its vicinity (e.g. the Calaveras Fault), the San Andreas Fault System is the most prominent as it runs through the majority of California, carries the largest slip rate, and marks the physical boundary between the Pacific and North American Plates. In this region alone, 30 earthquakes with Moment Magnitudes (Mw) >= 5.5 have been recorded over the past 100 years, with the most recent major event documented near the town of Parkfield in 2004 (M6.0) [ANSS Composite Catalog, obtained from the NCEDC, last accessed 2/18/2017]. Two of the largest events recorded in the region were the 1906 San Francisco and the 1857 Ft. Tejon Earthquakes with Mw estimated in the range ~7.8 – 8.0 [*Thatcher,* 1975; *Sieh*, 1978; *Hill et al.*, 1990], whose ruptures extended along the San Andreas to the northern and southern extents of the study region, respectively.

Along the length of the San Andreas Fault System, the slip behavior varies from fully locked to creeping. Continuous right-lateral aseismic slip of up to 30 mm/yr *Lisowski and Prescott,* 1981; *Argus and Gordon,* 2001] and frequent microseismic (Mw < 3.0) events [*Wesson et al.,* 1973] are observed where the fault creeps at the surface. In other sections the fault is locked where large (Mw >5.0) deep (10 – 15 km) events, but little continuous slip or microseismic events have been recorded [*Hill et al.,* 1990]. At the northern extent of the study region (Figure 1) the 1906 San Francisco rupture extends from the northern tip of the San Andreas to the town of San Juan Bautista, near the intersection

with the Calaveras Fault [*Allen et al.,* 1968]. Meanwhile, the 1857 Ft. Tejon rupture extends from the southern section of the study region (Figure 1) near the town of Cholame, CA (Figure 2) to roughly 350-360 km south near Cajon Pass, just northwest of the town of San Bernardino, CA [*Allen et al.,* 1968; *Sieh*, 1978].

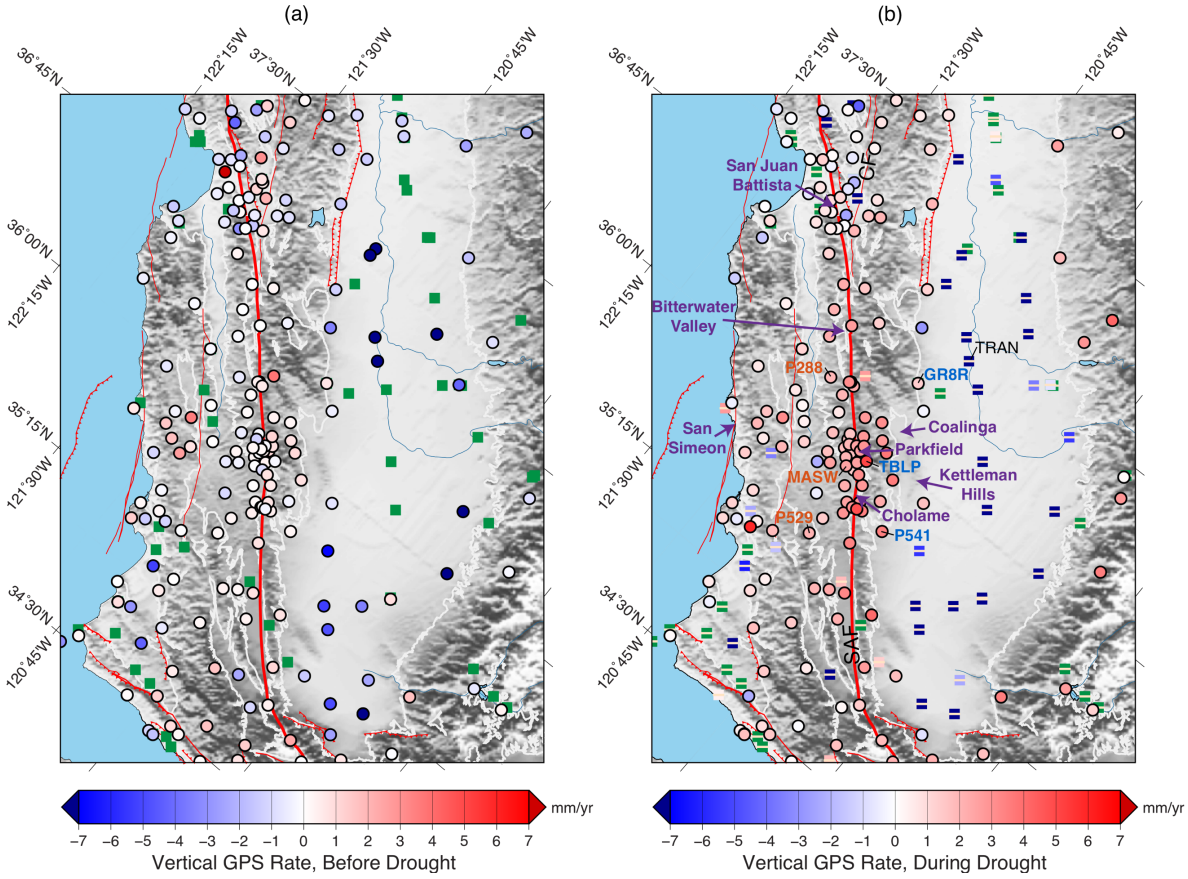

Figure 2 Distribution of vertical rates for GPS stations (colored from blue to red) in study area for the (a) before drought (2008 – 2012) and (b) during drought (2012 – 2016) periods. Those GPS sites that have been excluded because they are missing rates (mostly due to very incomplete time series) are colored green. Note that this map has been rotated from the purple-dashed region in Figure 1 to an oblique Mercator projection. Faults from USGS fault and fold database are drawn in red (labeled SAF – San Andreas Fault and CF – Calaveras Fault) and basin regions are outlined in white.

Additionally, (b) delineates which sites are included (circles) and excluded (white-dashed squares) for the analysis. Highlighted towns are listed in purple and stations stated in the manuscript are listed in orange, blue, and black. While the during drought vertical GPS rates clearly delineate between basin (blue circles) and bedrock (red circles), the before drought vertical GPS rates are not spatially conclusive.

In between the rupture extents of these two major events, the San Andreas Fault is known to creep aseismically. The actual extent of the creeping section is debated as creep rates can vary from ~18 – 30 mm/yr in the central section (between Bitterwater Valley and Parkfield, CA) to 1 to 20 mm/yr to the northwest (between Bitterwater Valley and San Juan Battista, CA) and southeast (between Parkfield and Cholame, CA) [*Burford and Harsh,* 1980] (towns denoted on Figure 2). Since several events of moderate magnitudes (4.0 – 6.0) have been recorded in these two regions of lower creep rates [*Hill et al.,* 1990], many refer to these localities along the San Andreas Fault as a transitional region between locked and creeping behavior [e.g. *Burford and Harsh,* 1980; *Harris and Segall,* 1987; *Titus et al.,* 2005; *Titus et al.,* 2011a]. Others propose that these transitional regions are in fact locked due to differences in stress in comparison to the high creep-rate section [e.g. *Schorlemmer and Wiemer*, 2005]. In addition to aseismic creep, the southern transitional creeping section is known to be home to repeating earthquakes and nonvolcanic tremor [*Nadeau et al.,* 1995; *Nadeau and Dolenc,* 2005; *Nadeau and Guilhem*, 2009].

Similarly, the nearby Calaveras, a vertical right-lateral strike-slip fault, slips in a fashion analogous to the transitional creeping regions of the San Andreas Fault. Creep rates for the section of the Calaveras Fault within the study region are in the range of 6 – 13 mm/yr [*Schulz et. al.,* 1982; *Galehouse and Lienkaemper,* 2003], such that creep accommodates a portion of the surface slip. Additionally, earthquakes of moderate magnitudes (4.0 – 6.0) [*Hill et al.,* 1990] have been recorded.

Most of the focal mechanism solutions along the San Andreas Fault within the Central California study region show right-lateral, near vertical dipping fault planes. However, some thrust mechanisms have been recorded on structures lying to the east, in

the vicinity of Kettleman Hills and Coalinga, CA [*Rymer and Ellsworth,* 1990] and to the west near San Simeon, CA [*McLaren and Savage,* 2001; *Hardeback et al.,* 2004] on northwest striking planes (locations denoted on Figure 2). While other thrust focal mechanisms exist to the south of the study area where the fault bends at an angle to the overall San Andreas Fault trend to form transpressional thrust faults [*Wesnousky,* 2005], almost all structures in the study region parallel the San Andreas Fault. Therefore, it has been suggested that these thrust mechanisms in the vicinity of the creeping section are a result of off-fault deformation from the change in slip behavior along the San Andreas Fault [*Titus et al.,* 2011a; 2011b].

Titus et al. [2011a] also suggested that differences in mechanical properties within the bedrock geology found in the Coast Ranges have an influence on the style and location of off-fault deformation and seismicity. The area to the northeast is a mix of sedimentary terrain of the Franciscan complex whereas southwest of the fault are mostly granites of the Salinian block [*Page,* 1981]. While only a few geologic structures have developed directly to the southwest of the fault and only within 5km of the trace, deformation in the sedimentary Franciscan block to the northeast is diffuse and is recorded up to 40km from the fault trace [*Titus et al.,* 2011a]. The heterogeneous nature in rheology between either side of the San Andreas has also been invoked to explain the observed asymmetric strain accumulation across the fault [*Schmalzle et al.,* 2006].

1.4 San Andreas Fault Strength

Numerous observations suggest that the San Andreas Fault is, with the exception of the creeping section, a strong seismogenic fault [*Scholz,* 2006]. Deep borehole friction measurements performed in the straight, locked, Mojave section of the San Andreas Fault

near Palmdale, California show a coefficient of friction (μ) of 0.45 at a depth of 0.85 km, which is thought to increase with depth [*McGarr et al.,* 1982]. Additionally, stress orientation measurements, derived from earthquake focal mechanisms, demonstrate an orientation angle of less than 60^{o} to the San Andreas Fault for σ_1 throughout the locked section of Northern California [*Provost and Houston*, 2003]. They suggest a high μ, similar to that of the surrounding crust. Therefore, the locked sections of the San Andreas Fault behave in a traditional "stick-slip" manner, with earthquakes occurring on preexisting faults due to an instability [*Scholz*, 2002]. Over the time-span of a rupture, the fault plane heals positively and shows velocity-weakening behavior, leading it to bond and regain stability [*Scholz,* 2002].

The existence and reasoning behind the San Andreas creeping section was of widespread debate until the completion of the SAFOD (San Andreas Fault Observatory at Depth) experiment. Although prevalent in subduction settings, the occurrence of creeping faults are extremely rare in continental localities [*Scholz,* 2006]. Here, stress orientations are markedly high (near normal to the fault) for the σ_1 component [*Provost and Houston,* 2003]. In contrast to hypotheses suggesting the possibility of high pore-fluid pressures at depth concentrated near the fault [e.g. *Rice,* 1992] and/or dynamic weakening mechanisms that reduce the dynamic friction during seismic slip [*Scholz,* 2006 and references therein], the SAFOD experiment confirmed the saponite material found in the active creeping section to be inherently weak [*Zoback et al.,* 2010; *Zoback et al.,* 2011]. Core extracted at depths of ~3 km from the two active localities of creep within the San Andreas fault zone, the Central Deforming Zone (CDZ) and Southwest Deforming Zone (SDZ), showed very

low frictional strength (μ~0.1 to 0.15) in laboratory experiments [*Lockner et al.,* 2011; *Carpenter et al.,* 2015]. The CDZ and SDZ core also exhibited velocity-strengthening behavior and near-zero to negative healing rates [*Lockner et al.,* 2011; *Carpenter et al.,* 2015]. Within 0.5 to 1 meter of these two local, active creeping zones, the μ of the wall rock increases abruptly to greater than 0.4 and shows velocity-weakening behavior [*Carpenter et al.,* 2015].

Over the past three decades, several authors have noted the existence of large serpentine outcrops at the surface in the active creeping section, but not the locked sections [e.g. *Allen*, 1968; *Irwin and Barnes,* 1975; *Page et al.,*1998]. However, the serpentine material found in these outcrops was still too frictionally strong to promote aseismic creep [*Scholz,* 2002]. The coefficient of friction was 0.2 at the surface and was thought to increase to $\mu = 0.4$ at seismogenic depths [*Scholz,* 2002]. With the discovery of saponite at depth, a smectite clay derived from the unique reaction of mg-fluids (from the serpentine) with quartzofeldspathic rocks concentrated in the Great Valley Sequence [*Lockner,* 2011; *Carpenter et al.,* 2015], the mystery of the active creeping section was solved. Additionally, *Moore and Lockner* [2013] were able to replicate this reaction in laboratory experiments, further confirming the fact that geology alone could explain the aseismic creeping section of the San Andreas Fault.

1.5 Central California Hydrology

Most of the water in California is stored within the 52,000 km^2 Great Valley aquifer, a large, deep structural trough filled with sediments as deep as 4 km [*Fliedner et al.*, 2000; *Faunt et al.,* 2009] within the study region. The section/profile across the Great Valley is structurally asymmetric as its base dips westerly such that the sediments are the

thickest at the basin's western edge, near the edge of the Coast Ranges [*Farrar and Bertoldi,* 1988; *Faunt et al.,* 2009]. The vast majority of fresh groundwater is contained in the upper 300 – 900 meters of the aquifer, except on the deeper western edge where fresh groundwater can exceed 1,000 meters depth [*Farrar and Bertoldi,* 1988; *Faunt et al.,* 2009]. Below the zone of freshwater is saline water, which is generally unusable for agricultural and drinking purposes. A steady supply of water to this region is vital for the Great Valley aquifer because agricultural products grown here are an important component of the United States economy. The Great Valley is often referred to as the "fruit and vegetable basket" of the United States [*Scanlon et al.,* 2012; *Bittman,* 2012]. In 2012, the market value of the Great Valley's farmed crops was $30 billion [*USDA Census of Agriculture*, last accessed 3/20/2017].

Within the Central California study region, the main water source comes from westerly winds carrying moist air from the Pacific Ocean during the winter months [*Farrar and Bertoldi,* 1988; *Carle,* 2016]. Due to topography, this precipitation is mostly deposited in mountainous regions as snow and/or rain from orographic lifting [*Alpert,* 1986; *Pandey et al.,* 1999]. This phenomenon, where air is cooled and moisture increases as it climbs over terrain, favors precipitation in orogenic belts [*Alpert,* 1986] mostly during the winter months (November to March) [*Faunt et al.,* 2009]. Mountainous localities such as the Sierra Nevada Range receive the largest yearly precipitation totals followed by the Coast Ranges, which sit at a lower elevation. These higher elevations see up to 85% of the state precipitation totals [*Faunt et al.,* 2009; *Scanlon et al.,* 2012]. The landscape of the Great Valley is low-lying and flat, contrasting greatly with the surrounding mountainous regions [*Planert and Williams,* 1995]. It receives very little direct precipitation and relies heavily

on runoff snowpack melt from the surrounding mountainous regions to satisfy its agricultural needs [*Planert and Williams,* 1995; *Faunt,* 2009]. This demand for water, however, is partially out of sync with runoff from the Sierra Nevada Range, especially in the midsummer months after the snowpack has entirely melted [*Carle,* 2016]. When surface water is no longer available, farmers will tap into groundwater aquifer resources for their agricultural needs.

Over the past 100 years the landscape of the Great Valley aquifer has been artificially altered to meet water needs across the entire state of California, with the construction of dams, aqueducts, and massive water diversion projects [*Scanlon et al.,* 2012; *Carle,* 2016]. This has dramatically changed the distribution of surface water loads throughout California. During times of extreme drought surface water from these diversion projects, along with direct precipitation and runoff from mountainous regions are not able to recharge the aquifers at adequate rates to accommodate state demands. Groundwater must then be pumped and depleted from underground aquifers [*Scanlon et al.,* 2012]. The response of the Earth to groundwater depletion (when demand exceeds supply) is extreme, measureable, subsidence [e.g. *Scanlon et al.,* 2012; *Faunt and Sneed,* 2015; *Farr et al.,* 2016]. This is detrimental to the seasonal renewability of the Great Valley aquifer, as excessive groundwater pumping compacts fine-grained (clay and silt) sediments permanently and severely reduces the aquifer's rechargeability [*Farrar and Bertoldi,* 1988; *Scanlon et al.,* 2012].

Droughts tend to have the largest effect on subsidence within the southern half of the Great Valley (spanning the majority of the Central California study region). In the southern Great Valley, reference evapotranspiration is the greatest (up to 140 cm/year)

[*Faunt,* 2009] due to hot, dry, summers, with temperatures frequently exceeding 100°F/38°C [*Durrenberger,* 1965]. Groundwater level changes measured from well data during the most recent drought for time periods Spring 2012 – 2013, Spring 2013 – 2014, and Spring 2014 – 2015, showed widespread decreases of up 300 cm over each one year period within the southern Great Valley [*California Department of Water Resources Data Library,* 2015]. *Farr et al.*, [2016] reported subsidence rates from InSAR satellite measurements of up to 58 cm between the period May 2015 – September 2016.

1.6 Seasonality in GPS and Seismic Observations

Several authors have previously noted seasonality in the context of GPS, InSAR, and seismic data. While it is hard to ascertain the seasonality of large magnitude earthquakes due to incomplete seismic catalogs at these magnitudes, micro-seismic events have been found to contain statistically significant recurring variations. *Dutilleul et al.,* [2015] used multifrequential periodogram analysis to resolve periodic intervals of 1 year, 6 month, and 4 months of earthquake occurrence along the San Andreas Fault near Parkfield, CA. The authors of *Dutilleul et al.,* [2015] didn't explore the spatial variability of the signal for this study, but did note a general increase in earthquake occurrence between August and November. *Christensen et al.,* [2007] analyzed a 21-year earthquake catalog of $M \geq 1.25$ in the Parkfield, CA region and provided monthly earthquake bins for both the creeping and southern transitional creeping sections (which the authors referred to as "locked"). Here the authors found general surges in seismicity between August and December, and general declines in seismicity between January and March. *McClellan*, [2015] analyzed $M \geq 6.4$ mainshocks for California between 1850 and 2011 and cited significant semiannual clustering of these large events in the spring and fall.

Similarly, several studies [*Borsa et al.,* 2014; *Amos et al.,* 2014; *Argus et al.,* 2014] have used data from GPS stations throughout the western United States to identify and model hydrologic-related influences of solid-Earth deformation. These studies focused solely on the vertical component of the GPS time series. *Roeloffs,* [2001] noted a seasonal signal in seven of the twelve creep meters crossing the San Andreas Fault near the town of Parkfield, CA. *Roeloffs,* [2001] attributed these seasonal signals to local perturbations in soil moisture due to factors such as vegetation and irrigation. In addition, the author noted surges in creep rates during rainy season and/or wet years.

Outside of California, *Heki* [2001; 2003] attributed the annual displacement of GPS sites to snow loads and suggested a relationship between increased seismicity during spring and summer in regions covered with snow in the winter. *Silverii et al*. [2016] looked at the seasonal deformation of karst aquifers in Italy using both horizontal and vertical GPS data. While the authors found the vertical GPS signal to related to an elastic mechanism via correlations with GRACE-water loading estimates, the horizontal GPS signal behaved poroelastically from hydrostatic pressure changes.

2

Data and Methods

2.1 Data and Processing

Previous work suggests a seasonal repeatability of peaks in seismic data [e.g. *Christensen et al.,* 2007; *Dutilleul et al.,* 2015]. We, therefore, are interested in understanding the crustal deformation patterns related to these periodic changes in seismicity. In order to achieve this goal, we use GPS data to document seasonal solid-Earth deformation within Central California and investigate its relation to nearby faults. We select an analysis timeframe of 2008 – 2016 to (1) compare and contrast seasonal signals from before (2008 – 2012) and during (2012 – 2016) the California drought (2) to avoid potential influences of postseismic relaxation from the 2004 M6.0 earthquake in Parkfield, CA. We do not consider analyzing data from before the 2004 earthquake because we found the stations to be too spatially sparse at distances >15 km from the fault to accurately constrain the long-wavelength, seasonal signals that we are after. Here, we formally define "seasonal" as any observed deformation within 25 km of the San Andreas Fault Zone that is not associated with long-term or drought-related trends.

Our primary study area encompasses the purple-dashed region in Figure 1. We additionally incorporate all available stations within the blue-dashed region to reduce the influence of edge effects and allow for full constraint of analysis within our study region. This GPS data is obtained from a variety of networks, processed at the Nevada Geodetic Laboratory (NGL) located within the University of Nevada, Reno (UNR), and aligned to the NA12 reference frame using GPS Inferred Positioning System (GIPSY) OASIS II software provided by the Jet Propulsion Laboratory (JPL). Because these processing methods have been documented previously [*Blewitt et al.,* 2013] and the conventions used

are documented on the NGL website (http://geodesy.unr.edu/gps/ngl.acn.txt, last accessed 2/19/2017) we do not further explain them here.

2.2 Observations from the Data: Example Baseline Time Series

We present observations which come directly from unfiltered, detrended, GPS data. We examine three pairs of GPS time series (GR8R+P288, TBLP+MASW, P541+P529) spanning the center of our study region and straddle three sections of the San Andreas Fault known to differ in behavior (station names and locations are denoted in blue and orange text in Figure 2). Each station was detrended using a singular MIDAS rate for the entire analysis period (2008 – 2016) and time series of baseline relative motion for each of these pairs (Figure 3) were constructed to obtain a basic understanding of how the North American and Pacific Plates seasonally move relative to each other.

From these observations, it is evident that most seasonal relative motion occurs perpendicular rather than parallel to the fault and the largest fault perpendicular motions are located near Parkfield in the southern transitional creeping section of the San Andreas Fault that runs from Parkfield to Cholame, CA (Figure 3b). While the main creeping section (running from Parkfield to Bitterwater Valley, CA) shows measureable fault perpendicular motion (Figure 3a), the locked section of the San Andreas Fault (south of Cholame) displays no measureable seasonal relative motion (Figure 3c). In addition, the southern transitional creeping section shows measureable fault parallel creep over the eight-year period, but the shape is generally parabolic and does not repeat annually (Figure 3b). For the remainder of this analysis, we will pay closest attention to the fault perpendicular signal because it is the most prevalent seasonal signal.

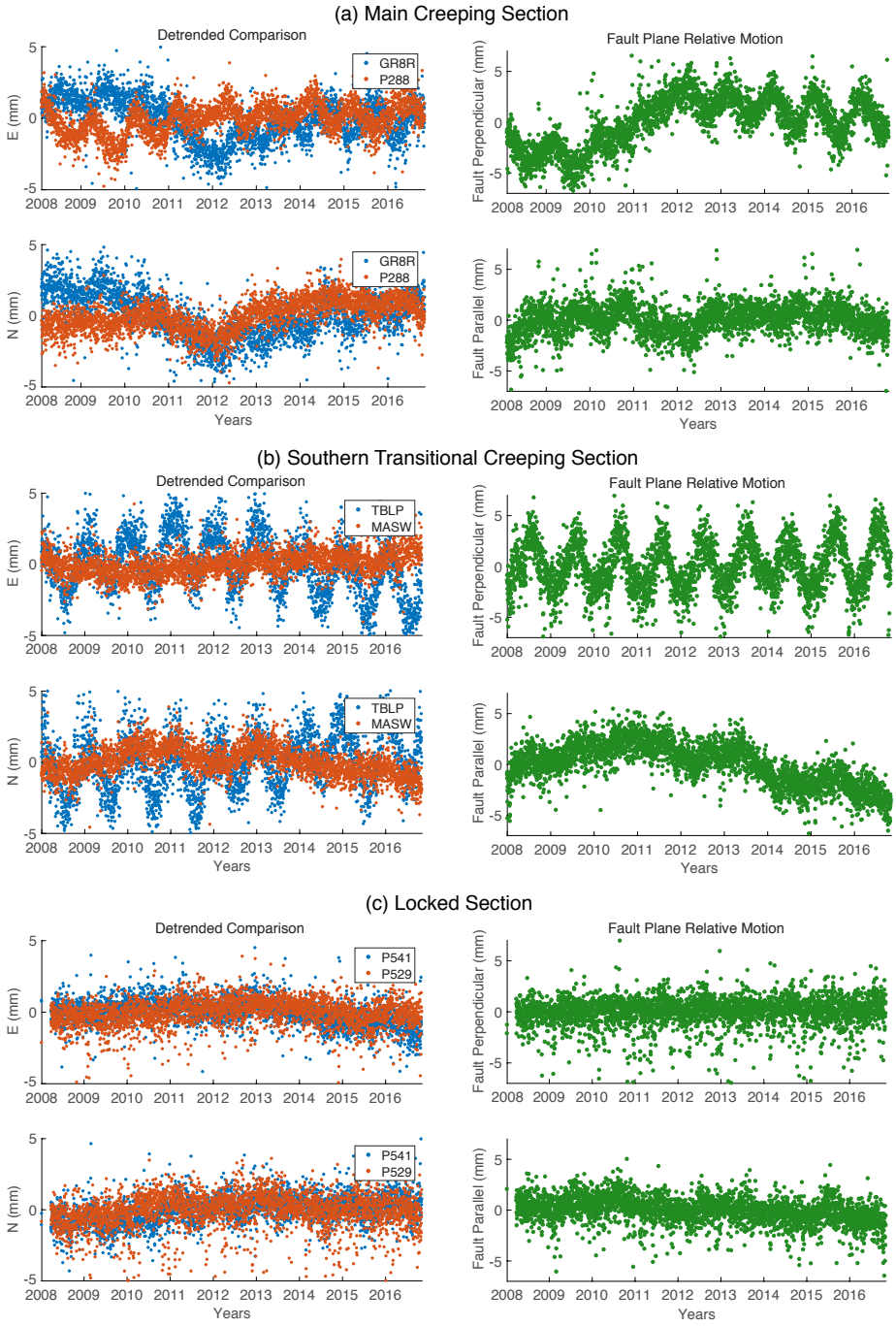

Figure 3 Detrended GPS time series (left) and their baseline relative motion (right) for three sections of the San Andreas Fault in Central California for the (a) Main Creeping Section, (b) Southern Transitional Creeping Section, and (c) Locked Section. Stations used are highlighted in Figure 2b in the color designated by the detrended time series. Convention here is negative fault-perpendicular contraction and positive extension. Right-lateral fault parallel motion is negative and left-lateral is positive.

2.3 GPS Station Selection

Geologic conditions dictate how GPS stations react to the presence of water. Such that we derive a seasonal signal related only to solid-Earth deformation signal, we want to rely on GPS stations located on bedrock rather than on unstable basin-fill. The removal of water from a porous sediment-filled basin will cause subsidence of a GPS station, whereas a GPS station located on bedrock will steadily rise in response to groundwater extraction of the nearby aquifer. For example, two time series, TBLP on bedrock and TRAN in the basin, are compared in Figure 4a and 4b (station locations shown in Figure 2). While TRAN is located in the heavily-pumped Great Valley aquifer and has been subsiding at 186 mm/yr from 2012 – 2016, TBLP has been rising at 5.1 mm/yr during the same period.

Aside from visually inspecting the aerial geology and station properties of the 369 GPS stations located within the blue-dashed region of Figure 1, we explored several properties of the GPS time series to understand the most systematic approach to select the GPS stations on bedrock. For the NA12 reference frame only, we first compared the vertical rate before and during drought derived by MIDAS, a robust trend estimator [*Blewitt et al.,* 2016] (Figure 2). We also examined the peak day of year phase derived from inverting for the long-term trend and annual/semiannual components of the time series for both the NA12 and IGS08 reference frames (Figures A1 and A2). In addition, we looked at the amplitude magnitude for the peak day of year from the inverted time series for both the horizontal and vertical components and the NA12 and IGS08 reference frames (Figures A1 and A2).

When comparing our results from these various methods in relation to the mapped basins available from the California Department of Water Resources, we found that the

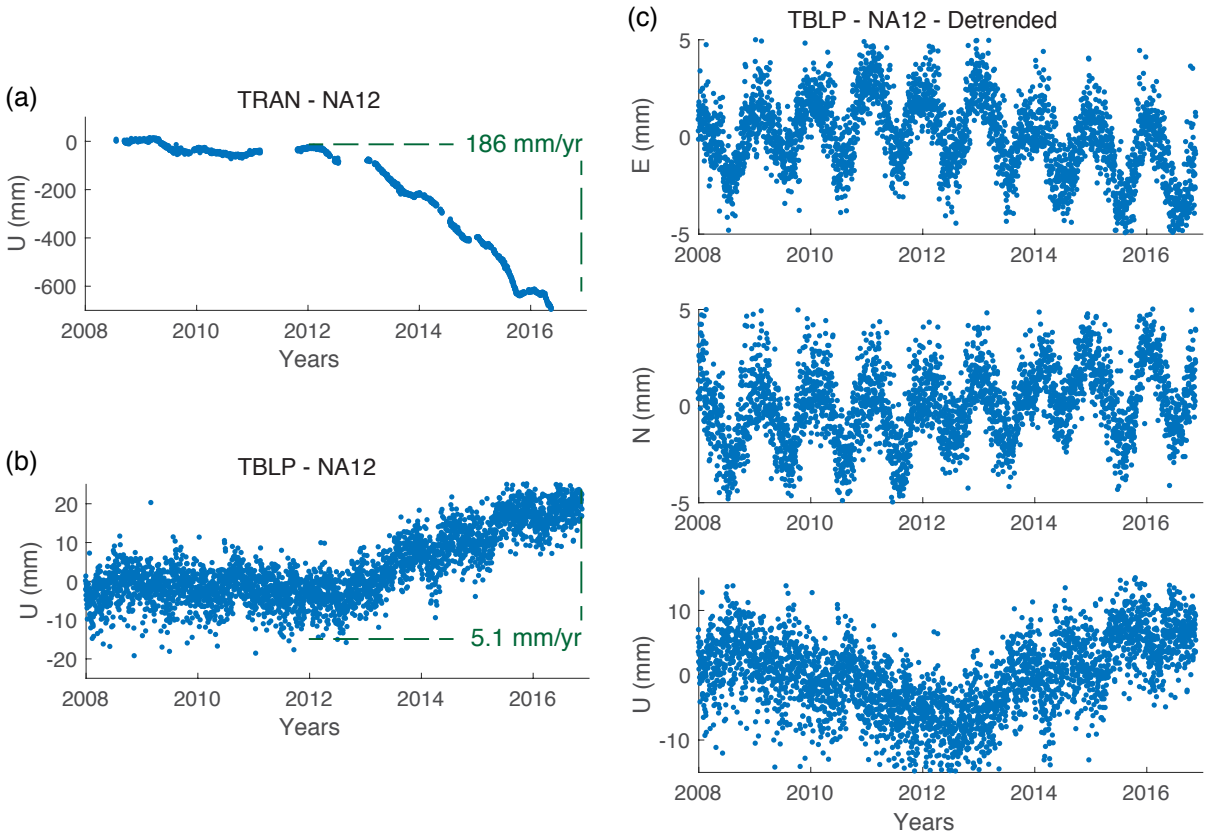

Figure 4 Up component of NA12 GPS time series for TRAN, located in the Great Valley, **(a)** and TBLP, located on bedrock near the San Andreas Fault **(b)**. The locations of these two stations are shown in Figure 2. All components of the TBLP time series detrended using a rate for the entire analysis period (2008 – 2016) is shown in **(c)**. It is evident here that (1) the seasonal signal is fairly consistent throughout and (2) detrending using a single rate is not enough to obtain a seasonal time series centered about zero.

peak day of year and the amplitude magnitude for the peak day of year for both the IGS08 and NA12 reference frames (Figures A1 and A2) showed more scatter and were less conclusive than the NA12 vertical rates. While the vertical GPS rates for before (Figure 2a) and during (Figure 2b) drought periods for the NA12 reference frame can spatially delineate the boundary of the Great Valley of California, the before drought rates are unable to delineate the difference between the bedrock and smaller basin regions in the study

region. However, the existence of the drought period in the vertical GPS data provides the clearest picture of identifying the bedrock stations to be used for analysis.

Ultimately, the vertical rate cut-off for inclusion of stations in analysis is based on the normally-distributed section of the during drought rates (red-dashed inset, Figure 5b). A histogram of all vertical GPS rates for both periods is shown in Figure 5. While the before drought vertical rates show a fairly normal-distribution (Figure 5a), the during drought rates are long-tailed (Figure 5b). The negative outliers in the long-tailed distribution extending out to -300 mm/yr is the property of the during drought signal which makes it easy to distinguish stations on basin-fill (heavily-subsiding) from bedrock (in the range not-subsiding to rising) (Figure 5b). Roughly 89% of stations containing during drought rates (and 72% of all stations in the study area) lie within the normally distributed during drought rates of -5 mm/yr to +5 mm/yr.

It is important to note that the MIDAS trend estimator will automatically exclude determining a rate for stations with short time series or possessing too many steps. If the station did not meet MIDAS criteria for both the before and during drought periods, the station was automatically eliminated (59 total). For stations missing a during-drought rate, but having a pre-drought rate only (12 total) the aerial geology was inspected to see if the location was on bedrock. However, none fit this criterion so they were eliminated. This analysis was performed before drawing the during drought rate histogram.

Of the 298 total GPS stations containing a during drought rate we automatically eliminate all stations subsiding at rates $\geq$ 5.0 mm/yr from further analysis (32 total). For stations subsiding at rates between 1 and 5 mm/yr (35 total), strict criteria were used to only include stations if they could be confidently identified as a deep drilled station through

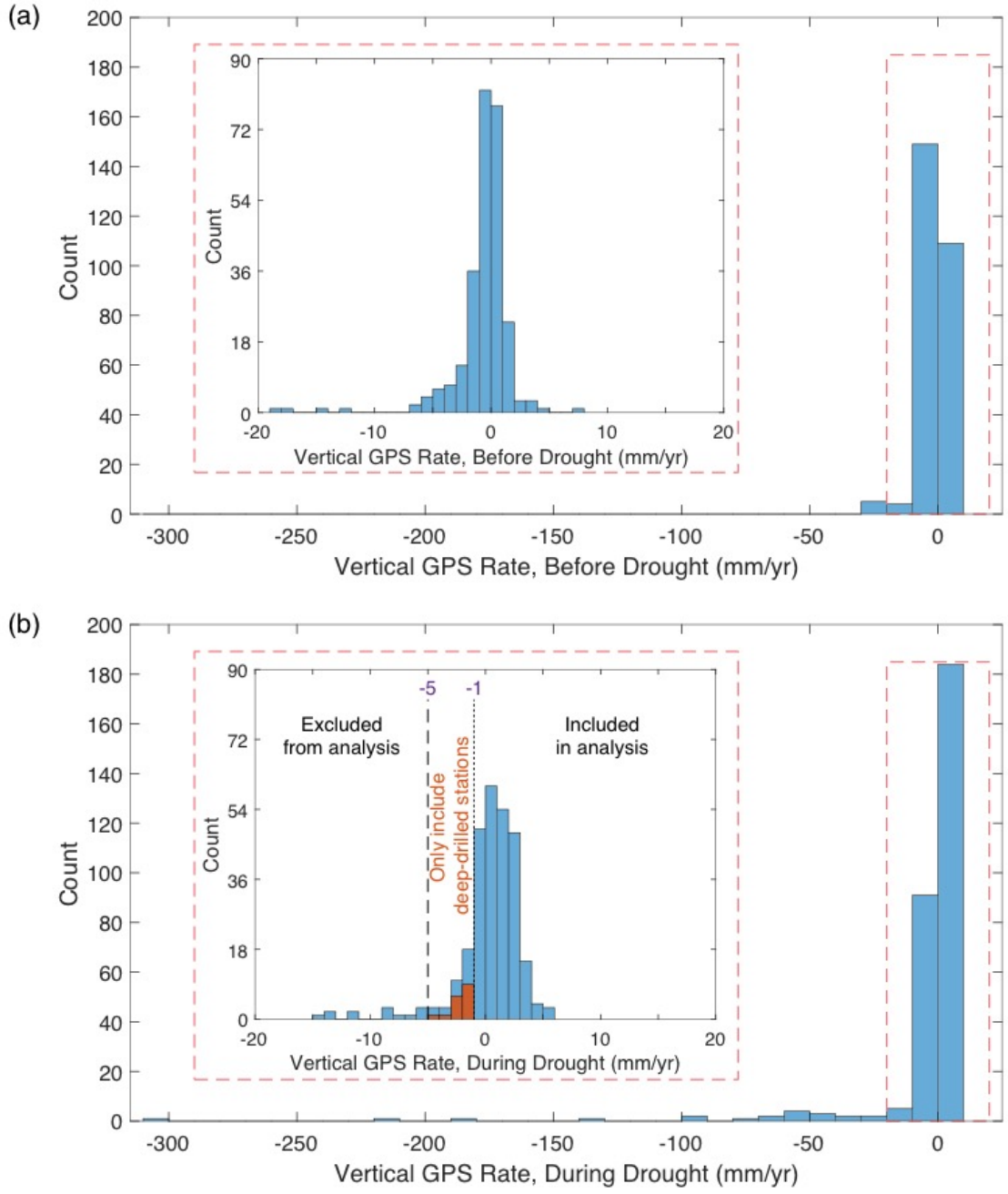

Figure 5 Histogram of vertical GPS rates for (a) before drought (2008 – 2012) and (b) during drought (2012 – 2016). The inset histogram is for the dataset dashed in red in the main histogram and shows in greater detail the normally distributed portion of the data. Using the (b) inset, we automatically eliminate all GPS stations subsiding at rates ≥ 5.0 mm/yr during the drought. For stations subsiding at rates between 1 and 5 mm/yr, strict criteria is followed to only include GPS stations if they could be identified as a deep-drilled station. The red bars are distribution of deep-drilled stations with 1-5 mm/yr subsidence rates.

clear documentation provided by the station owner (17 stations fit this criterion and were included). Additionally, stations meeting the above criteria, but containing known problems and incomplete time series not detected by MIDAS (16 total) were excluded from the analysis. This left 232 stations for use in our analysis, which are listed in Table A1.

2.4 Characterizing the Seasonal Signal

Upon examination of the 232 accepted GPS time series located on bedrock, we found several signals to be prevalent in the GPS time series – namely those from seasonal changes, long-term (un)loading from the California drought, long-term tectonic motion, among several less pronounced features. From this visual inspection, the majority of the time series contain differences in rates in the pre- and during-drought periods, in all components of the time series (east, north, and up), but very little variation in the seasonal signal. For example, when comparing the vertical components of TBLP (on bedrock) and TRAN (in a basin), shown in Figures 4a and 4b, drought effects are mainly seen in their trends. In investigating the TBLP time series detrended using a singular rate for the entire 2008 – 2016 time period (before + during drought), the horizontal seasonal amplitude and period remains fairly steady throughout. At this station, the data shows that the drought has had little effect on the seasonality of the GPS signal.

In addition to the vertical GPS signal, the horizontal component is slightly affected by drought trend effects and these trends must be removed in order to extract the seasonal signal. Simply detrending the GPS time series using one rate for the entire 2008 – 2016 time period is not enough to eliminate trends (e.g. Figure 4c). We first correct for these effects by detrending using two MIDAS rates, one for the before (2008 – 2012) and one

for the during (2012 – 2016) drought periods. We then solve for the annual and semiannual components of the time series using a weighted inversion described by

$$x(t) = \mathrm{H}(\mathrm{t} - t_o) + C_1 \cos(\omega t) + S_1 \sin(\omega t) + C_2 \cos(2\omega t) + S_2 \sin(2\omega t) \quad (1)$$

where C_1, C_2, S_1, S_2 are the annual and semiannual terms, t is the time, t_o is a vector of time(s) at given step(s) in the time series, $\omega = 2\pi/T$ such that T is the period in years (for our purposes $T = 1$), and H is the Heaviside step function. For the Heaviside step function, we automatically assume a hard-wired step at $t_o = 2012.0$ or the transition point marking the start of the drought. We additionally reference a master steps database derived from the IGS log files associated with the GPS stations and earthquake data (available through the Nevada Geodetic Laboratory – *http://geodesy.unr.edu/NGLStationPages/steps.txt*, last accessed 8/15/2016) to identify other times (t_o) when steps may have occurred due to factors such as equipment maintenance or an earthquake.

To assure the correctness of each modeled time series, we visually inspect the accuracy of each GPS time series model in reference to the input time series. We correct for steps in the time series that are missing from the steps database as well as phase and amplitude errors. An example of the seasonal modeling procedure and the associated residuals for TBLP is shown in Figure 6. In addition, a summary of RMS model fitting statistics are shown in Table 1.

In choosing the modeling method for seasonal trend extraction, we must note additional approaches. Others have widely used the *Cleveland et al.* [1990] Seasonal Trend LOESS (LOcally wEighted Scatterplot Smoothing) formally known as the STL method [e.g. *Bergmann et al.,* 2012; *Borsa et al.,* 2014; *Lafare et al.,* 2016] to decompose time series into seasonal, trend, and residual components. This procedure relies on an iterative

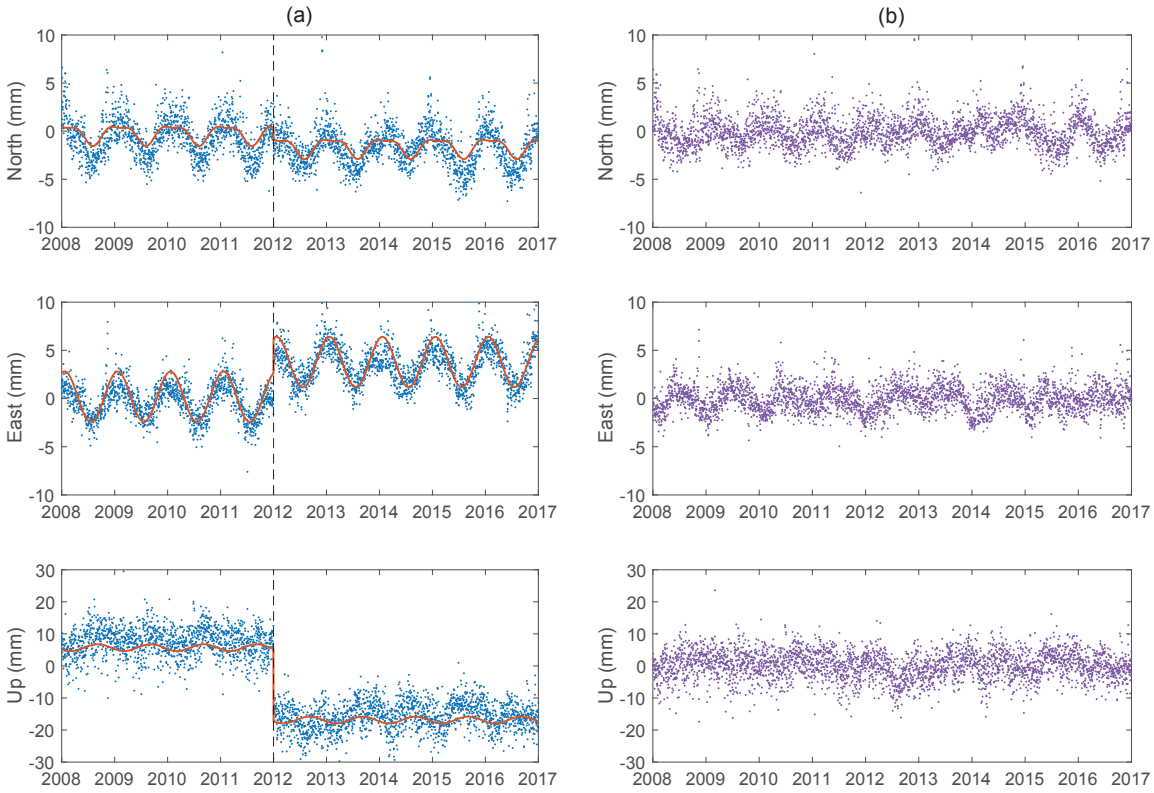

Figure 6 Example of seasonal time series extraction for TBLP. **(a)** Time series detrended using two rates for before (2008 – 2012) and during (2012 – 2016) the drought (blue) and the model fit to the detrended time series (orange). The hard-wired step at 2012.0 is denoted as a black-dashed line. **(b)** Residual between detrended and modeled data.

Direction	***RMS Model Deviation***		***RMS Scatter***	
	Mean	Median	Mean	Median
East	1.3534	1.094	1.4332	1.1442
North	1.3165	1.2028	1.371	1.2557

Table 1 RMS deviation between the measured detrended destepped time series and the seasonal (annual + semiannual) model, as well as the RMS scatter of the detrended destepped time series. The mean and median of all RMS values, which were obtained for all stations selected for use in the analysis, are summarized above.

weighted neighbor regression procedure and has been shown to be fairly robust. Another approach is to apply a high-pass filter to detrended GPS time series that will pass the annual and semiannual signals (frequencies more than 1/year) and remove frequencies less than the annual cycle. In the case of this study these lower, removed, frequencies would include signals related to biases as well as trends from the drought. Variations of this technique have been explored by a couple authors [e.g. *Langbein,* 2004; *Jin et al.,* 2010; *Davis et al.,* 2012].

The main caveats to the above two methods are that they require a complete, gap-less time series and cannot produce an overall seasonal signal for the analysis timeframe. While they can better account for sharp dives in the seasonal signal during periods of water extraction and replenishment, our visual inspection of the model in relation to the data has, for the most part, covered this issue. We also have numerous GPS stations with gaps of several months to years and would be unable to use this data if we were to apply the other two methods.

2.5 Using GPS Imaging to Derive a Robust Seasonal Displacement Field

Seasonal displacements are obtained by sampling the annual + semiannual model derived from (1) at each of the twelve months of the year. We despeckle the seasonal displacements by applying a median spatial filter algorithm called GPS Imaging [*Hammond et al.,* 2016] to the horizontal components of the selected station time series. The GPS Imaging method can be best described as a hybrid approach between geostatistical kriging [*Krige*, 1951; *Matheron*, 1963] and median spatial filter image processing techniques. This procedure is applied (separately) to the east and north components of the time series for all selected stations. The result of filtering is to remove

outliers/noise while preserving coherent, spatial signals in the dataset. An additional benefit of the GPS Imaging technique is that it can output filtered displacements onto any evaluation point, including points on a predefined, gridded field. When placing the output from GPS Imaging into a strain modeling algorithm this mitigates the effect of outliers. The gridded input also eliminates artefactual alternating zones of extension and compression near active fault structures [e.g. *Hackl et al., 2009; Baxter et al., 2011; Titus et al., 2011a*], known to occur from large spatially heterogeneous networks.

In applying the GPS Imaging algorithm to the selected bedrock stations, we make several minor modifications to the original published procedure described in *Hammond et al.,* [2016] to accommodate our smaller, more focused, research area and goals. For a given GPS station in a network, the algorithm selects the nearest neighbors to that station, derived from a Delaunay triangulation of the site positions on a sphere [*Delauna*y, 1934; *Renka*, 1997] and takes a weighted median of the neighbors to determine the filtered signal for that GPS station. Because stations closer together are more likely to move in a similar manner, contributing displacements are weighted as a function of distance from the evaluation point to the stations connected via the Delaunay triangulation. The weights are empirically derived and summarized in a one-dimensional spatial structure function (SSF), which represents how the data variability changes with distance, analogous to a semivariogram in kriging [*Hammond et al.,* 2016].

The final imaged displacement field can be sensitive to the SSF. For example, an SSF function which drops off to zero too quickly at short distances (e.g. blue line, Figure 7) will fit the outliers of the input data. At the other end of the spectrum, a SSF function which equals one at all distances (e.g. orange line, Figure 7) will equally weight all of the

nearest sites when calculating the median. The SSF function described in the *Hammond et al.,* [2016] study (black line, Figure 7) was empirically derived for vertical GPS rates over a length-scale of California and Nevada and singular time frames. For this study we have twelve time frames (one for each month of the year) and three potential directions (east, north, and displacement magnitude). We derive the SSF function from the data for these three directions at the two peak times of the year, February and September (light-yellow lines, Figure 7). Our final SSF function is the median of these six SSF's (yellow line, Figure 7).

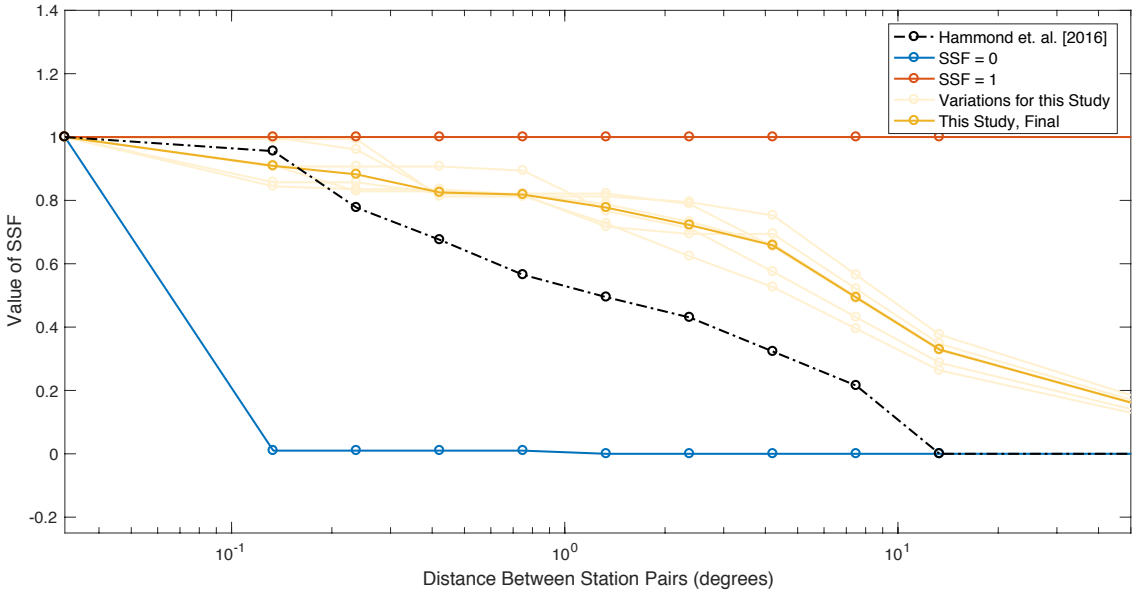

Figure 7 Spatial Structure Function (SSF) used for GPS Imaging algorithm (dark yellow line) in comparison to that used in *Hammond et. al.* [2016] (black dashed line). The six SSF's which were statistically derived from the three component (East, North, and Magnitude) analysis for the two peak periods (February and September) are shown as light yellow lines. The final SSF for this study (dark yellow line) is the median of the six light-yellow lines. In addition, an SSF that drops off to zero too quickly at short distances such that it fits the outliers is shown with the blue line and one that equally weights the nearest sites to each GPS station is shown with the orange line.

Using the SSF function derived for this dataset, for a given month of analysis, we arrive at our final gridded displacements by first taking the weighted median seasonal displacement at each GPS station of the nearest neighbors (for an example see Figure 8). We then apply this same algorithm using these filtered displacements as input and output evaluation points located at the knotpoints of our strain model grid. Each of these two steps are performed separately for the two directions of displacement (east and north).

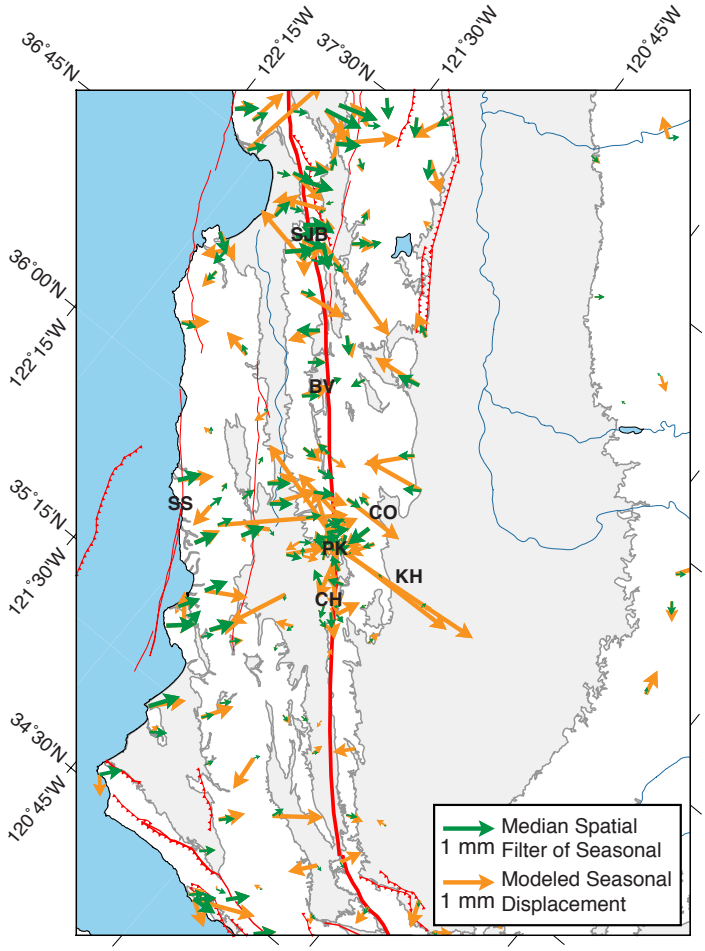

Figure 8 Example of median spatial filter technique (GPS Imaging) applied to seasonal GPS displacements for the month of February. The orange vectors are the seasonal displacements for February and the green vectors are the median-spatial filtered displacements. Locations San Juan Battista (SJB), San Simeon (SS), Bitterwater Valley (BV), Parkfield (PK), Cholame (CH), Coalinga (CO) and Kettleman Hills (KH) are denoted. Faults are drawn in red, rivers/oceans in blue, and basin locations obtained from the CA Department of Water Resources are shaded in gray.

The gridded filtered seasonal displacements obtained from the output of the GPS Imaging algorithm (Figure 9) display the seasonal displacement field at two separate seasons: the end of the wet period (February) and the end of the dry period (September). In comparing these two displacement fields, we notice three main patterns along the San Andreas Fault, (1) between Bitterwater Valley and Cholame, CA (main creeping and southern transitional creeping sections), seasonal displacements near the fault generally imply contractional strain in the wet period and extensional strain during the dry period. (2) South of Cholome, CA in the locked section of the fault, displacements vary minimally across the fault during both periods of time. (3) Between Bitterwater Valley and San Juan Bautista, CA (northern transitional creeping section) the displacements generally imply extensional strain during the dry periods and contractional strain during the wet periods. However, in this section, the signal is less pronounced than between Bitterwater Valley and Cholame, CA.

In addition, displacements to the east of the Great Valley along the foothills of the Sierra Nevada Range display spatially cohesive patterns. These seasonal filtered gridded displacements generally point toward the east during the wet period (February) and toward the west during dry period (September). This general pattern is consistent with elastic displacements from surface snow loads in the high Sierra Nevada Range, pulling higher elevation stations toward the Sierra Nevada Crest (eastward) in February. It is important to note the poor station coverage of this region in comparison to along the San Andreas and Calaveras Faults. The GPS displacement images are not as well constrained in the Sierra Nevada, owing to their being fewer and more geographically sparse stations.

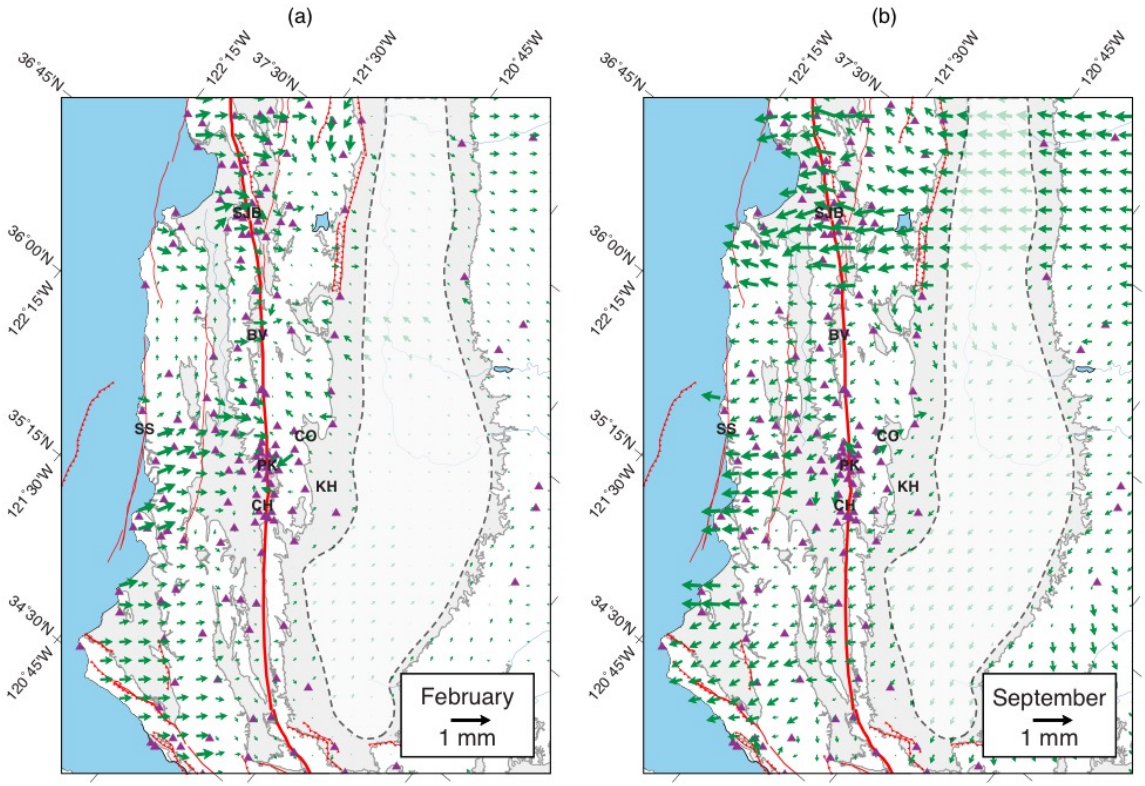

Figure 9 Gridded GPS Imaged example displacements (green vectors) for (a) February (wet season) and (b) September (dry season). Locations San Juan Battista (SJB), San Simeon (SS), Bitterwater Valley (BV), Parkfield (PK), Cholame (CH), Coalinga (CO) and Kettleman Hills (KH) are denoted. Faults are drawn in red, rivers/oceans in blue, GPS stations in purple, and basin locations obtained from the CA Department of Water Resources are shaded in gray. Also, denoted over the Great Valley (semi-transparent dashed-polygon) is the region where displacements were eliminated from input into the strain model due to lack of data.

2.6 Strain Model Derivation

For each month in the year, we utilize these filtered seasonal gridded displacements obtained from the GPS Imaging algorithm [*Hammond et al.,* 2016] to construct a strain model after the approach of *Holt et al.,* [2000]. We build an analysis grid for the strain model, which has been set up to directly parallel and center over the central section of the San Andreas Fault. This helps to avoid any unexpected deformation artifacts in the output strain model near the fault. As mentioned in the previous section, the input seasonal gridded

displacements are located at the knotpoints of this rotated analysis grid. However, we eliminate displacements in the grid for regions within the Great Valley where no bedrock GPS stations are available to constrain the GPS Imaging median spatial filter. The extent of the eliminated input region is designated by the dashed, semitransparent polygon shown in Figure 9.

To estimate strain from the gridded displacement field we derive a continuous horizontal velocity field, $u(\hat{x})$, using a least squares inversion [*Holt et al.,* 2000].

$$u(\hat{x}) = r(\boldsymbol{W}(\hat{\boldsymbol{x}}) \times \hat{x} + \boldsymbol{\omega} \times \hat{x}) \quad (2)$$

where $\boldsymbol{W}(\hat{\boldsymbol{x}})$ is a rotation vector function that is expanded using bi-cubic Bessel spline interpolation [*deBoor*, 1978] acting along a curvilinear grid, *r* is the earth radius, $\hat{x}$ is a unit vector of direction cosines of each point on the Earth's surface [*Haines and Holt,* 1993; *Haines et al.,* 1998], $\boldsymbol{\omega}$ is the rotation that transforms the input displacements into a best-fit (least-squares sense) frame, and × denotes the cross product. To find $\boldsymbol{W}(\hat{\boldsymbol{x}})$, we must minimize the following objective function

$$\sum_1^N \left(\bar{\varepsilon}_{ij}^{model} - \bar{\varepsilon}_{ij}^{obs}\right)\left(\bar{\varepsilon}_{pq}^{model} - \bar{\varepsilon}_{pq}^{obs}\right)(V)_{ij,pq}^{-1} + \sum_1^M \left(u_i^{model} - u_i^{obs}\right)\left(u_j^{model} - u_j^{obs}\right)C_{ij}^{-1} \quad (3)$$

where $\bar{\varepsilon}_{ij}^{model}$ is the average value of modeled/fitted strain in each grid area, $\bar{\varepsilon}_{ij}^{obs}$ are the observed strains (we set this to zero because we don't have input strain/earthquake data), $V_{ij,pq}$ is the a priori variance-covariance matrix, u^{obs} are the input filtered seasonal gridded displacements from the GPS Imaging algorithm, u^{model} are the output modeled displacements along the same points as the input filtered seasonal gridded displacements, C_{ij} are the uncertainties in displacements within the input filtered seasonal gridded

displacements, N are the number of grid areas, and M are the number of velocity observations.

For every cell in our grid lying within mapped sections of the San Andreas Fault and the Calaveras Fault, we set a constraint to the model where we expect most of the strain for the area to be directly accommodated on the San Andreas and Calaveras faults. This constraint is set by the variance – covariance matrix, $V_{ij,pq}$, which adjusts the probability of expected strain rate for the San Andreas and Calaveras Faults. We set a high apriori standard deviation for grid cells containing faults and a comparatively low apriori standard deviation for all other grid cells. This idea is analogous to assuming that the fault is weak in comparison to the surrounding crust. However, because we are trying to fit this fault condition in addition to the input filtered seasonal gridded displacements, there is a trade-off between fitting the data and fitting the condition of the model. We discuss this trade-off further in section 3, and ultimately choose a final model which fits both the data and the model constraint within a 95% confidence threshold.

Even though our seasonal gridded displacements from the GPS Imaging algorithm are reference frame independent, one condition of the model is that a frame is chosen. We define our reference frame to be a fixed Pacific Plate, by constraining the derivatives of $\boldsymbol{W}(\hat{\boldsymbol{x}})$ to be zero for the most westerly grid points (located in the Pacific Ocean). However, to deal with the issue of reference frame independence we solve for a rotation simultaneously with solving for the spatial derivatives of $\boldsymbol{W}(\hat{\boldsymbol{x}})$, such that strain in the area of the Pacific Plate is minimized. By solving for a rotation vector insures the minimization of the strain rate model. We find that this rotation is typically fairly small. Although the reference frame that we choose does not matter for this study, in the future we would like

to potentially incorporate total strains and this setup is what we would need for these types of displacements.

Once we have $\boldsymbol{W}(\hat{\boldsymbol{x}})$, the modeled horizontal seasonal strain field, ε, are the spatial derivatives of $\boldsymbol{W}(\hat{\boldsymbol{x}})$, which are formally defined as,

$$\varepsilon_{\phi\phi} = \frac{\hat{\Theta}}{\cos\theta} \cdot \frac{\partial \boldsymbol{W}}{\partial \phi} \tag{4}$$

$$\varepsilon_{\theta\theta} = -\hat{\Phi} \cdot \frac{\partial \boldsymbol{W}}{\partial \theta} \tag{5}$$

$$\varepsilon_{\theta\phi} = \frac{1}{2}\left(\hat{\Theta} \cdot \frac{\partial \boldsymbol{W}}{\partial \theta} - \frac{\hat{\Phi}}{\cos\theta} \cdot \frac{\partial \boldsymbol{W}}{\partial \phi}\right) \tag{6}$$

where θ is the latitude, ϕ is the longitude, $\hat{\Theta}$ is a North pointing unit vector, and $\hat{\Phi}$ is an East pointing unit vector. We also define dilatational strain as $\varepsilon_{\phi\phi} + \varepsilon_{\theta\theta}$ and shear strain as $\sqrt{\left(\varepsilon_{\phi\phi} - \varepsilon_{\theta\theta}\right)^2 + \left(\varepsilon_{\theta\phi}\right)^2}$.

3

Results

3.1 Verifying the Strain Model Setup

We verify the setup of our strain model by testing two sets of synthetic data for circumstances which have a known result. We run two tests; one for displacement parallel and the other for perpendicular to the central San Andreas Fault. For both tests, we input synthetic displacements of the same magnitude and direction at the knotpoints of our strain grid for the North American Plate. We set all displacements on the Pacific Plate to zero and eliminate synthetic input displacements for locations where they were also eliminated from the main strain solution due to lack of data (gray-shaded region, Figures 10, 11, 12). This setup forces the condition that strain only occurs along the San Andreas Fault.

We use the methodology described in section 2.6 to derive the strain field from the synthetic data. Our results show that both the synthetic parallel (Figure 10) and perpendicular (Figure 11) displacements produce expected output strain solutions. For the synthetic parallel displacement test (Figure 10), we find that most strain is accommodated in the shear, rather than dilatational strain component. The only sections where dilatational strain is documented is at bends/deviations from the main trend of the central San Andreas Fault. Additionally, most of the strain axes along the San Andreas Fault are the same magnitude for both the directions of maximum contraction and extension. This verifies the dominant shear component for the case of synthetic parallel input displacements. For the synthetic perpendicular test (Figure 11), we find that most strain is accommodated in the extensional dilatational, rather than the shear strain component. Throughout the entire section of the San Andreas fault a minimal amount of shear strain is recorded, however the strain axes point towards extension perpendicular to the San Andreas Fault. The strain axes show little to no magnitude in the maximum contraction direction.

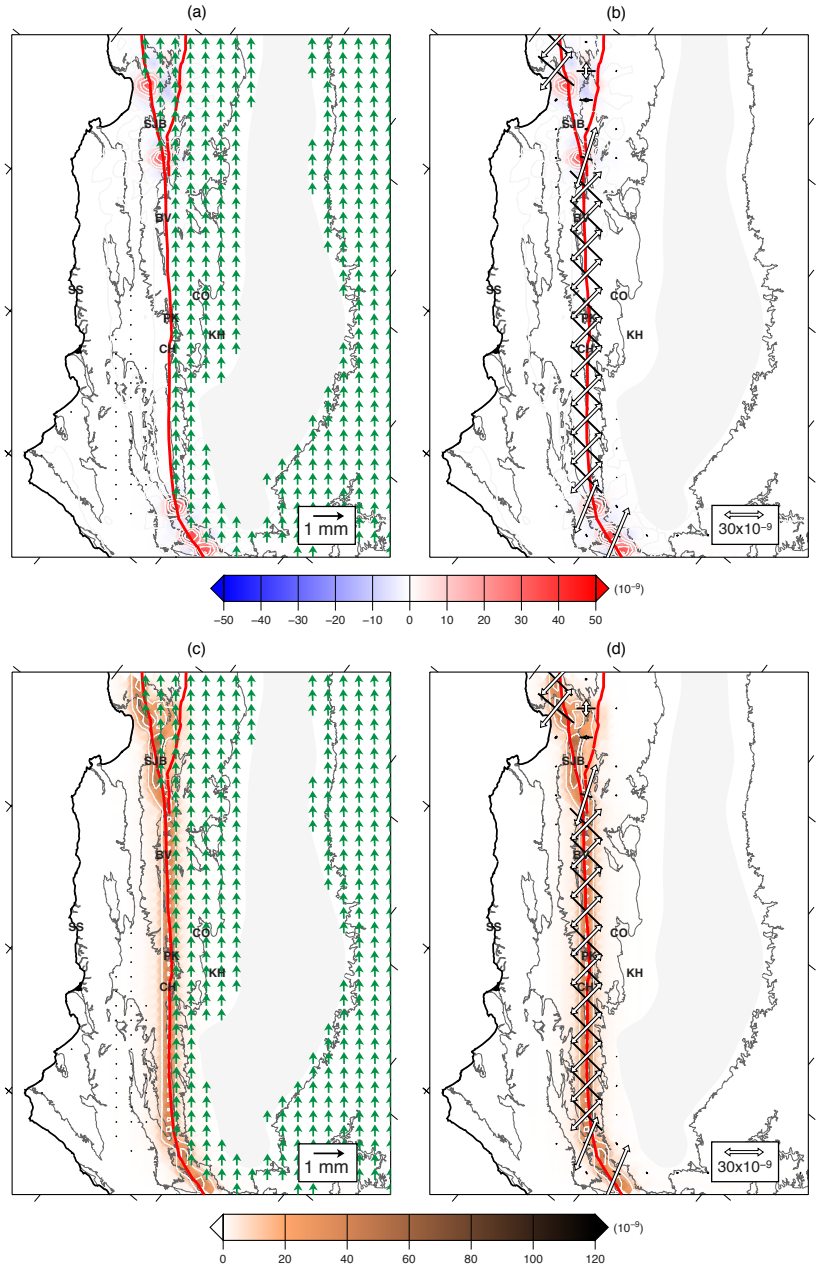

Figure 10 Synthetic test of strain accumulation using displacements that parallel the central segment of the San Andreas Fault for (a + b) dilatational strain and (c + d) shear strain. (a + c) show the synthetic input gridded displacements (green vectors), which are located at the knotpoints of the strain grid. All displacements located west of the San Andreas Fault are zero and the region where displacements were eliminated from the main strain solution (Figure 12) due to lack of data (gray-shaded region), were also eliminated for this test. (b + d) show the strain axes, using the convention of black as maximum contraction and white as maximum extension. Faults, basins, and locality annotations are same as annotated in previous figures.

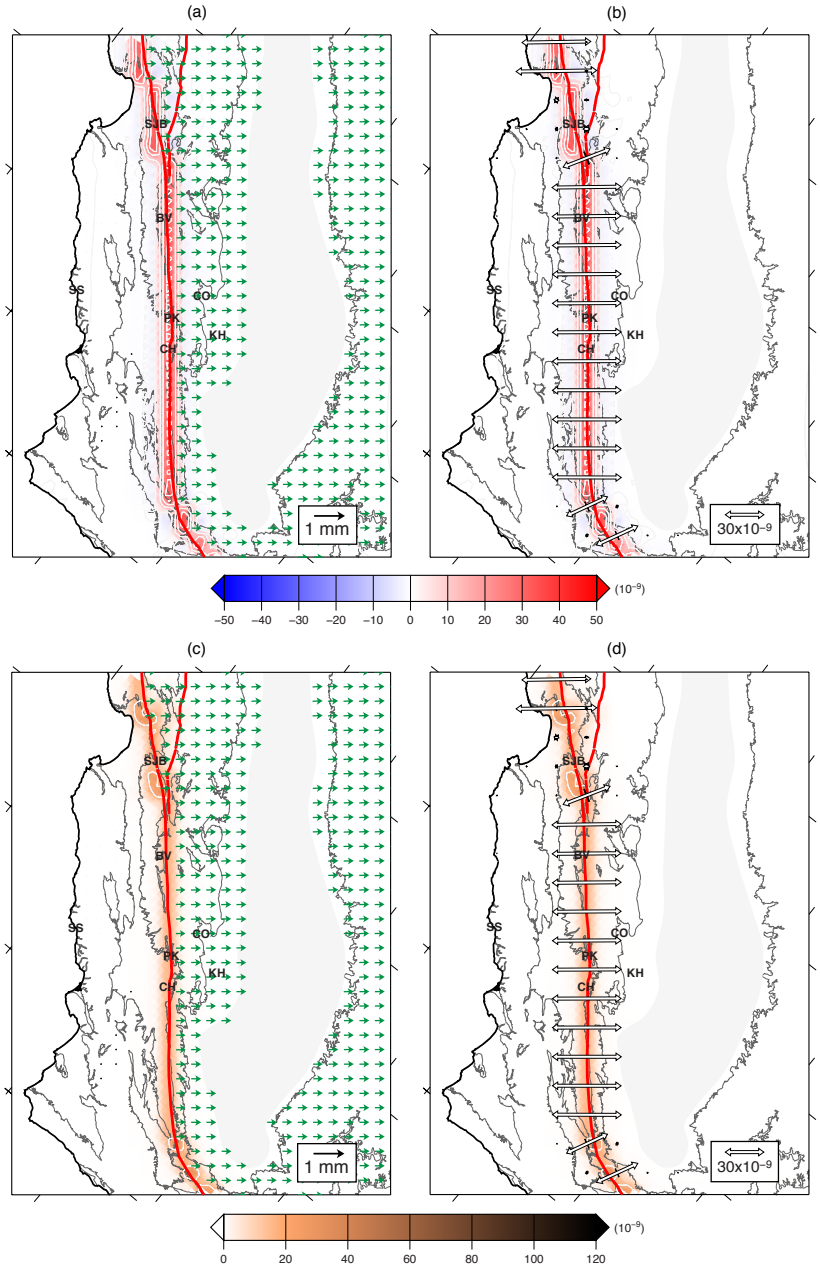

Figure 11 Synthetic test of strain accumulation using displacements perpendicular to the central segment of the San Andreas Fault for (a + b) dilatational strain and (c + d) shear strain. (a + c) show the synthetic input gridded displacements (green vectors), which are located at the knotpoints of the strain grid. All displacements located on the Pacific Plate are zero and the region where displacements were eliminated from the main strain solution (Figure 12) due to lack of data (gray-shaded region), were also eliminated for this test. (b + d) show the strain axes, using the convention of black as maximum contraction and white as maximum extension. Faults, basins, and locality annotations are same as annotated in previous figures.

Our synthetic tests (Figures 10 and 11) show that the condition where most strain is accommodated on the San Andreas and Calaveras Fault strands works when the condition is forced. However, in reality a good portion of strain is accommodated near, but off of these two fault strands. We test three different cases of strain accommodation by varying the apriori on and off-fault standard deviations, which adjusts the probability of expected strain rate for the San Andreas and Calaveras Faults.

Only in the most extreme case of a very low off-fault standard deviation (1.5), is the condition of the model fully enforced. Here the fault is very weak relative to the surrounding crust, such that all strain must occur on, rather than near or off of the San Andreas and Calaveras Faults (Figure A3). On the other hand, with the case of a high off-fault standard deviation (4.0) a larger portion of strain is accommodated off of the fault. This solution is mostly dictated by the data alone and is close to a homogeneous solution where all standard deviations in the variance-covariance matrix are equal (Figure A4). We compare the root mean squared (RMS), weighted root mean squared (WRMS) and reduced χ^2 of all three solutions in Table 2. We choose a final strain model which accommodates both the condition suggested by the model and that suggested by the data (Figure 12), using on and off-fault standard deviations of 1,250 and 2.5, respectively. This solution has an average reduced χ^2 of ~2.19 over all twelve months, which is within 2σ or 95% confidence (Table 2).

Figure 12a

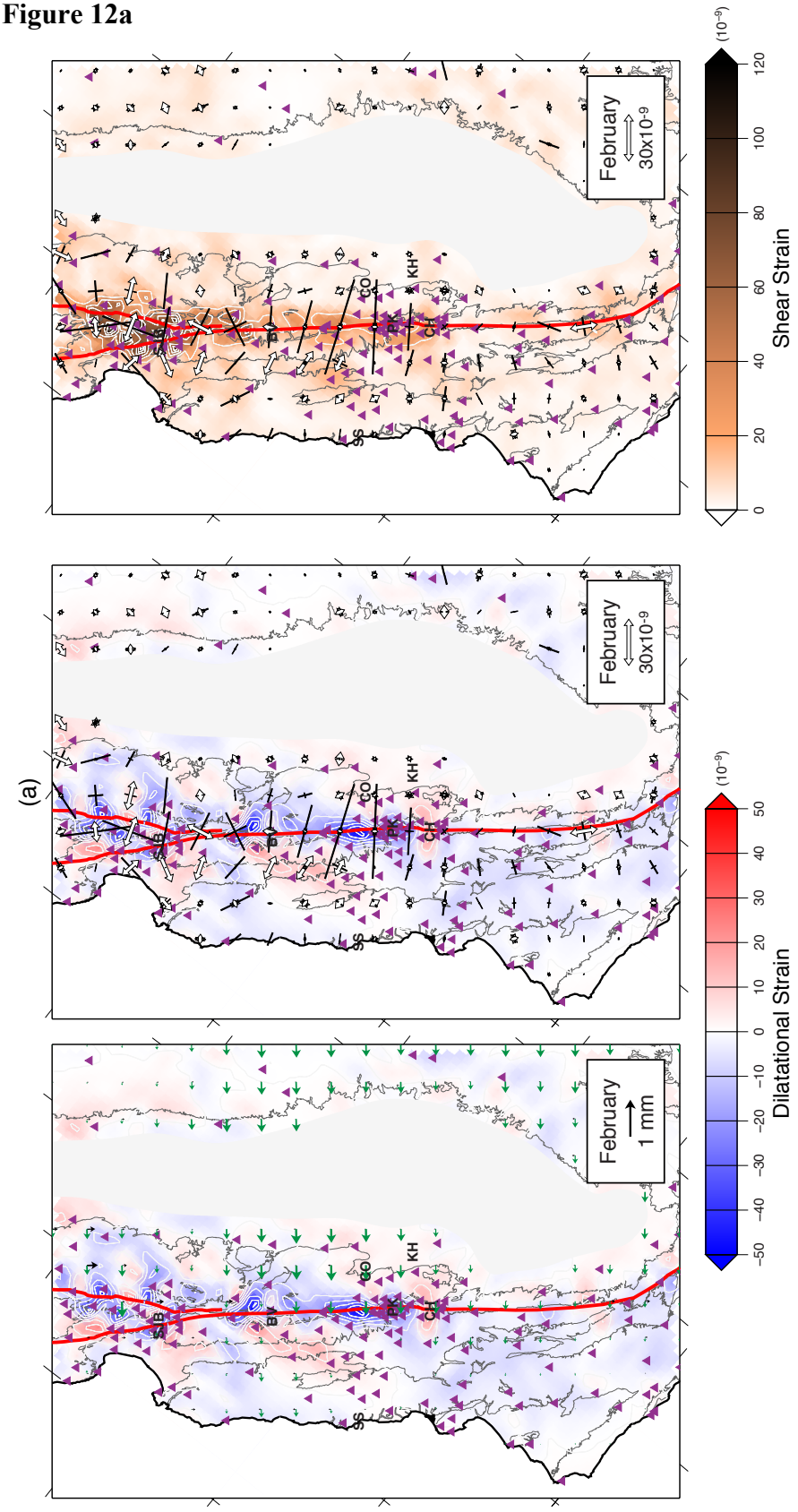
(a)
February
30x10⁻⁹
February
30x10⁻⁹
February
1 mm
(10⁻⁹)
Shear Strain
0
20
40
60
80
100
120
(10⁻⁹)
Dilatational Strain
50
40
30
20
10
0
−10
−20
−30
−40
−50
SS
BV
CO
KH
PK
CH

Figure 12b

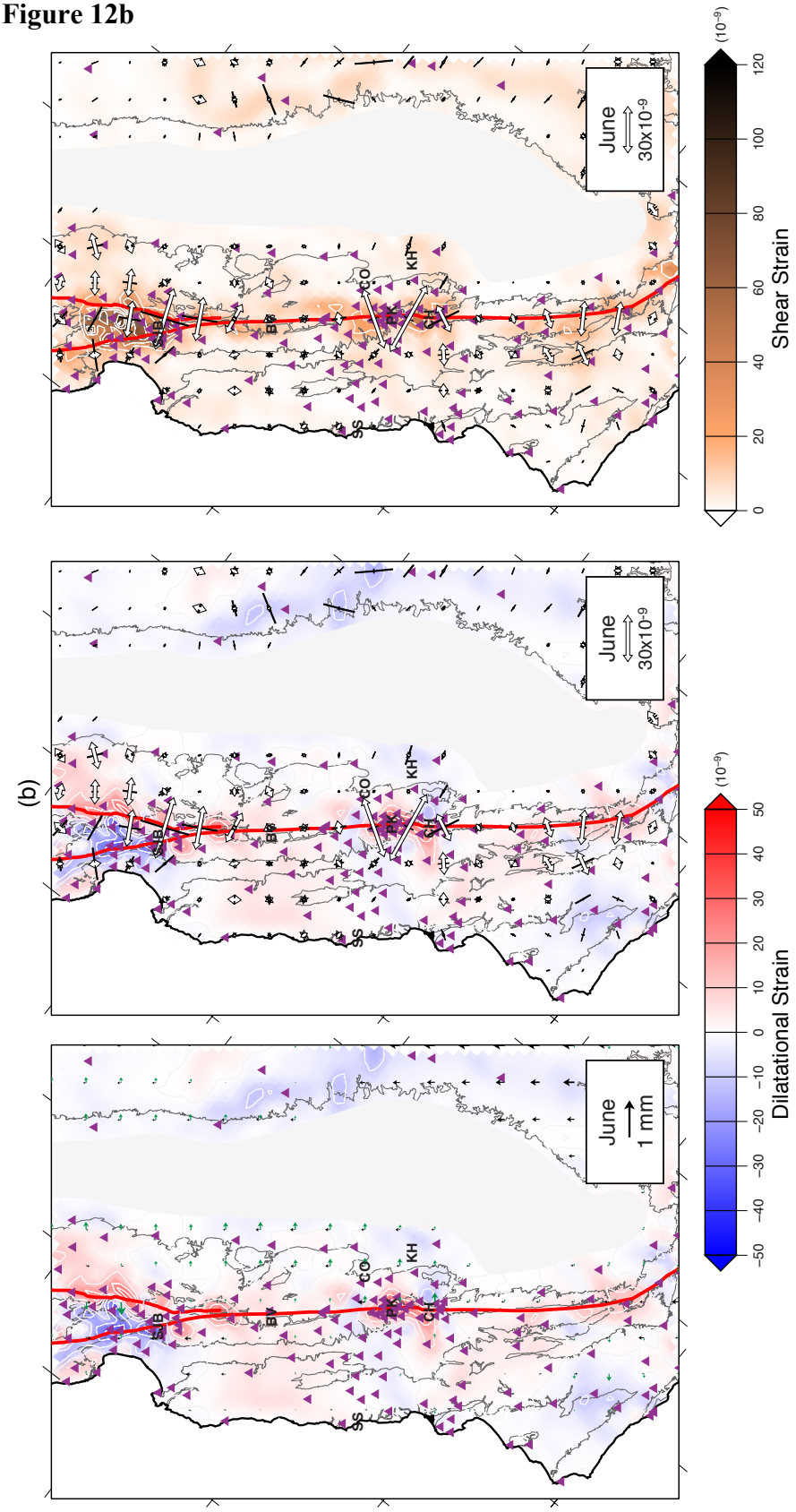
(b)
June
30x10⁻⁹
June
30x10⁻⁹
June
1 mm
SS
BK
CH
KH
CO
Shear Strain
Dilatational Strain
(10⁻⁹)
0
20
40
60
80
100
120
50
40
30
20
10
0
−10
−20
−30
−40
−50

Figure 12c

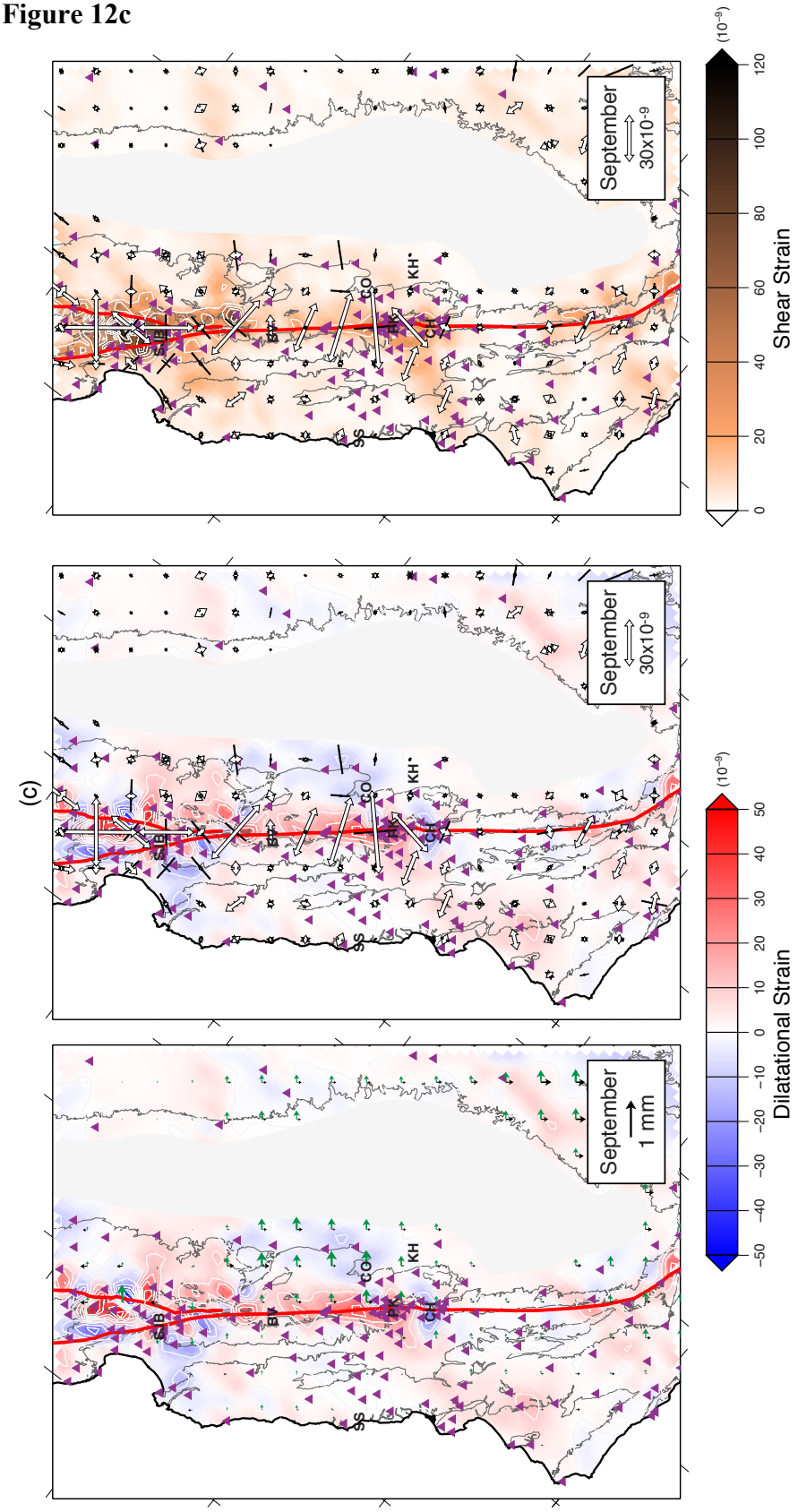
(c)
September
30x10⁻⁹
September
30x10⁻⁹
September
1 mm
Shear Strain
Dilatational Strain
(10⁻⁹)
(10⁻⁹)
0
20
40
60
80
100
120
−50
−40
−30
−20
−10
0
10
20
30
40
50
SS
CH
PK
BK
CO
KH
SB

Figure 12 (Three previous pages) Models of dilatation (left and middle panels) and shear (right panel) strain for **(a)** February, **(b)** June, and **(c)** September. The far-left panel of each month (a – c) shows modeled displacements in a Pacific reference frame, which have been decomposed into fault normal (green vectors) and fault parallel (black vectors) motion. This is the model using a ratio of 500:2.5 of on-fault to off-fault standard deviations. The middle and right panels display the principle strain axes, using the convention of black as maximum contraction and white as maximum extensional. The region where input gridded filtered displacements were eliminated from the solution due to lack of data (gray-shaded region) has been covered over by a white polygon. Stations, faults, basins, and locality annotations are same as annotated in previous figures.

On Fault	***Off Fault***	***RMS***		***WRMS***		***Reduced χ^2***	
		Mean	Median	Mean	Median	Mean	Median
2000	**4.0**	0.0374	0.0376	1.0292	1.0346	1.0751	1.0705
1250	**2.5**	0.0511	0.0514	1.4693	1.4768	2.1924	2.1810
750	**1.5**	0.0662	0.0664	1.9559	1.9581	3.8863	3.8340

Table 2 Root mean squared (RMS), weighted root mean squared (WRMS), and reduced χ^2 values for the mean and median of all months (January – December) for each ratio of on vs off fault standard deviations. The 1200-2.5 model (beige row) was used as the final model for this study.

3.2 Final Strain Model Results

Our final strain model shows a variety of patterns throughout the study area. For each of the three strain solutions, we extract twelve time series of dilatational and shear strain along the San Andreas and Calaveras Faults (Figures 13 and 14). The most notable feature occurs between Parkfield and Bitterwater Valley along the main creeping section of the San Andreas Fault. This section shows a peak extensional (positive dilatational) strain lobe in August/September and a peak contractional (negative dilatational) strain lobe in February/March. The north transitional creeping zone along the San Andreas Fault

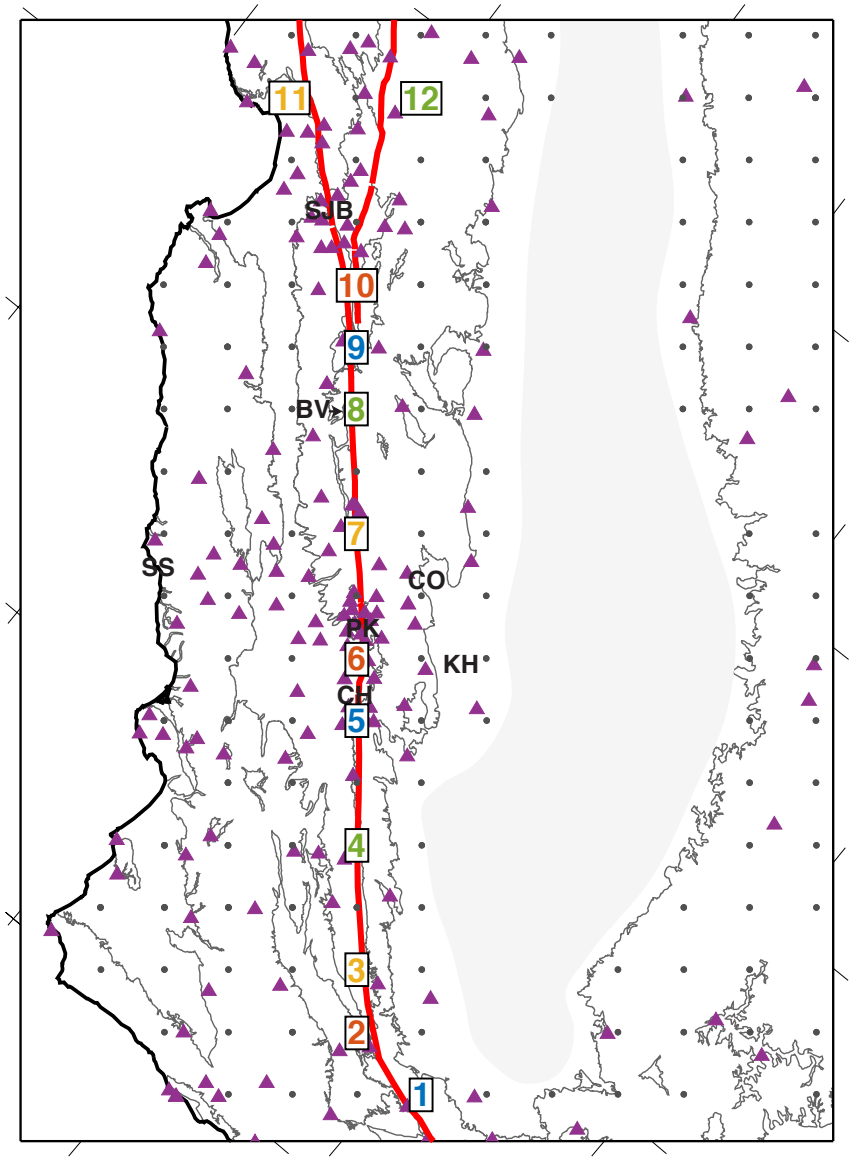

Figure 13 Key for locations of strain time series shown in Figure 14. The color of the number in this figure matches the color of the line in Figure 14. Black dots denote the strain axes locations from Figure 12 and are the possible locations for time series extraction. Locations, faults, GPS stations, and basins are same as previous figures. Black dots denote location where time series could be extracted from and is synonymous with the axes locations. The gray-shaded region denotes where GPS stations were eliminated from the main strain solution due to lack of data.

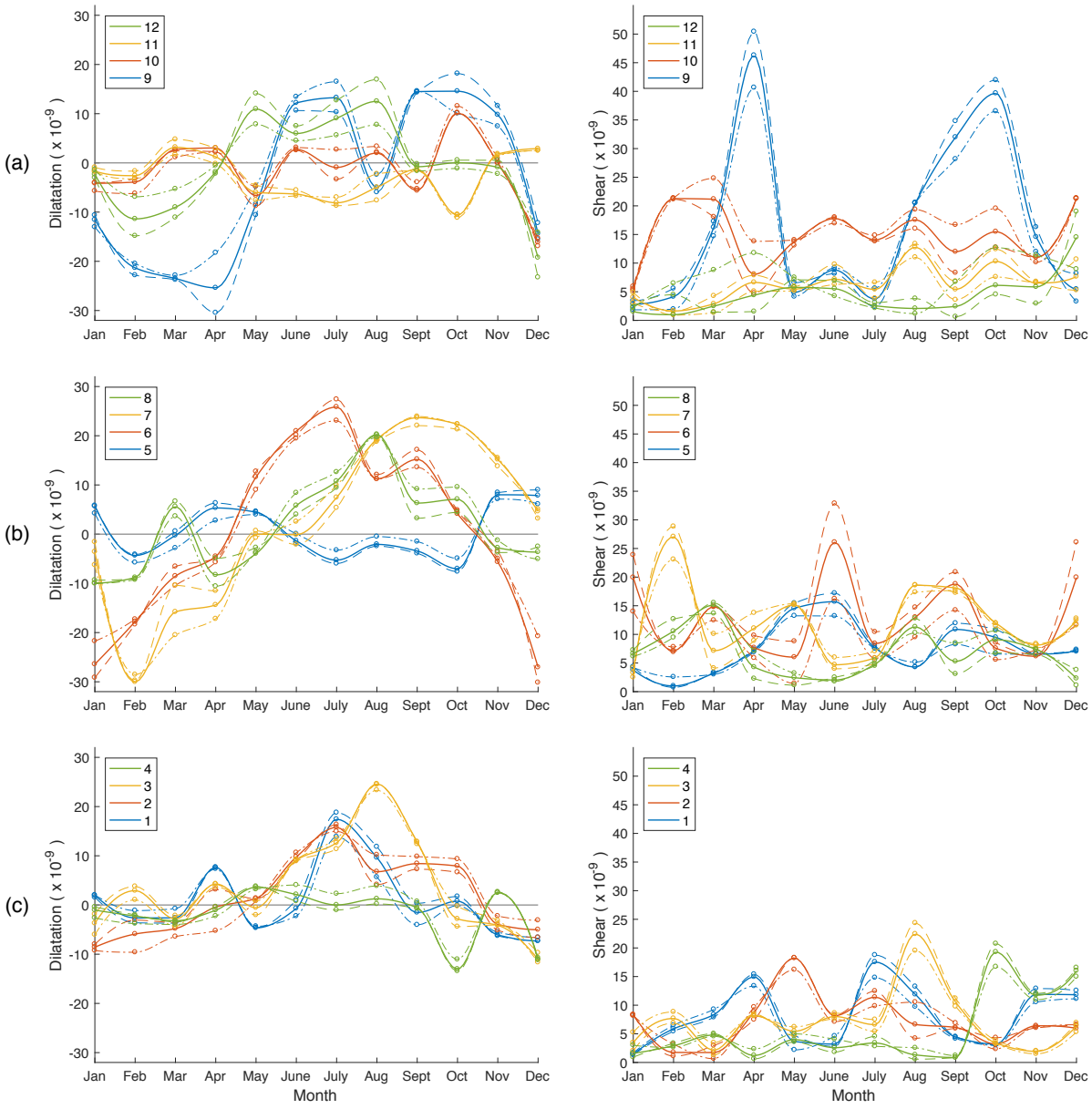

Figure 14 Time series of the dilatation (left) and shear (right) strain for the **(a)** North, **(b)** Central, and **(c)** Southern sections of the Central California study region. Locations for each time series is denoted on Figure 13 in the same color text as the lines in these diagrams. The three lines for each location denote the different scaling ratios for on/off fault standard deviations with 125:1 as dashed, 200:1 as solid, and 500:1.5 as dash-dot.

(running from Bitterwater Valley to San Juan Battista) and the Calaveras Fault display general similarities with the trend found along the main creeping section. North of San Juan Battista along the San Andreas Fault, the region generally shows an opposing dilatational strain pattern with peak extensional strain in February/March and contractional strain in September. Moving south, the southern-half of the southern transitional creeping section (running from Parkfield to Cholame) shows an opposing anomaly to the main creeping section with extensional strain in February/March and contractional strain in August/September. For the most part the locked section starting south of Cholame shows little evidence of seasonality. However, a small extensional strain anomaly appears in the strain time series and the strain axes in June.

Although most of the significant strain signal in the study region lies in the fault normal/dilatational strain component, shear strain is localized in several distinct areas. The strain axis just north of Parkfield shows a small shear strain signal in September. Additionally, shear strain is localized in the region between the San Andreas and Calaveras Faults in both the February, June, and September strain maps. The strain time series show significant peaks in shear strain in April and September/October at node number nine, where the San Andreas and Calaveras Faults intersect.

In addition to the preferred setup which uses fault locations to constrain the location of strain, we present a model that only considers filtered seasonal gridded displacements as input. In other words, the model contains equal apriori standard deviations for all grid cells. This model (Figure A5) shows some similarities to the preferred model. Specifically, the general trend of contractional strain during the wet period of February and extensional strain during the August/September dry season localized on the main creeping section of

the San Andreas Fault, prevails in the homogenous model. Additionally, the opposing anomaly in the southern-half of the southern transitional creeping section (running from Parkfield to Cholame), the general lack of strain in the locked San Andreas Fault south of Cholame, the existence of a small peak in extensional strain in June where the San Andreas Fault bends at the southern extent of the study area, and the general existence of similar dilatational strain patterns on the creeping Calaveras in retrospect to the main creeping San Andreas Fault all hold true in the homogeneous model (Figure A5).

The most notable difference between the preferred and homogeneous models lies in the region between the Calaveras and San Andreas Faults. While the preferred model places large strain magnitudes between the two fault strands, the magnitudes of strain within the homogenous model are in accord with the entire study region. Also, the large shear strain anomaly at node nine (intersection of the San Andreas and Calaveras Fault) in April and September/October found in the preferred model is virtually non-existent in the homogeneous model. It may be that when fault locations are set within several grid cells of each other, the model requires a finer resolution grid to properly resolve the signal.

Another point to note regarding all strain models presented in this work are the advantages and disadvantages of using the GPS Imaged displacements as input. While the GPS Imaging algorithm is optimal for clarifying the direction of the seasonal signal, the full magnitude of the signal is not fully represented in the strain models. Rather this is a robust, highly conservative, filtered version of the seasonal signal. If seasonal displacements were not filtered before being inputted into the strain model, magnitudes of strain could reach up to double the values quoted in this study.

4

Discussion

It is evident from these results that a seasonal signal exists along the San Andreas and Calaveras Faults in Central California. The most prevalent seasonal signal occurs between Parkfield and Bitterwater Valley, which comprises the main creeping section. This region shows peaks in contraction during the wet period (February/March) and peaks in extension during the dry period (August/September). In sharp contrast, seasonality is generally not observed in the locked section south of the town of Cholame. Additionally, the southern transitional creeping section shows two distinct patterns. For the most part this region, between Parkfield and Cholame, shows peaks in contraction during the wet period (February/March) and peaks in extension during the dry period (August/September), similar to the main creeping section. However, the segment of the southern transitional creeping section surrounding the town of Cholame opposes this trend with peaks in extension during the wet period and peaks in contraction during the dry period.

In similarity to the main creeping section, the *Christiansen et al.* [2007] study shows general surges in seismicity between August and December, and general declines in seismicity between January and March. They analyzed 21 years of microseismicity binned monthly for both the creeping section and the south transitional creeping section (which they generally referred to as "locked" in their study). For the future, their study can be improved by directly correlating the location of peaks in seasonal strain from this study with binned seismicity for each localized region. A peak in an annual (12 month) earthquake periodicity was reported by *Dutilleul et. al.,* [2015] in the Parkfield, CA region and showed a general surge in earthquakes during August-November. The authors, however, did not investigate the spatial variability of the signal. *McClellan*, [2015]

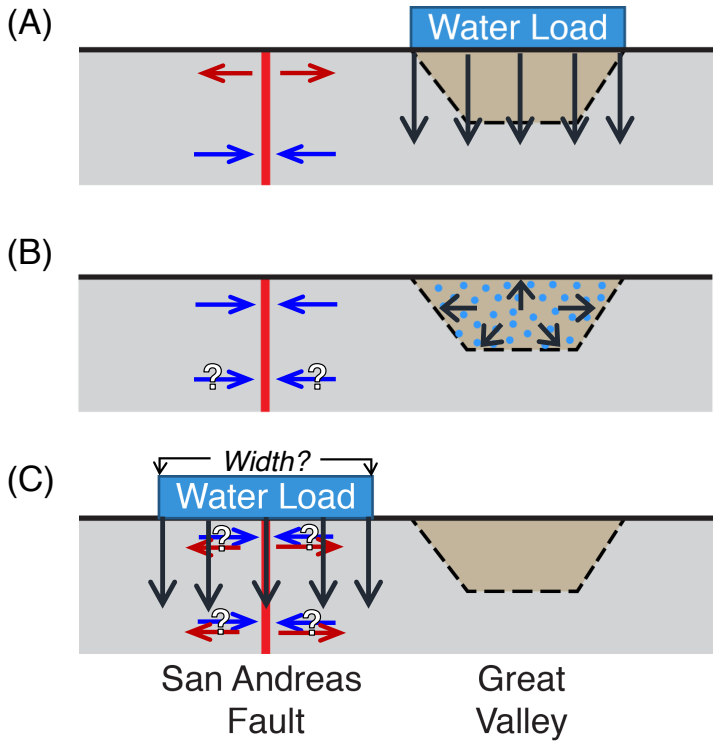

Figure 15 Possible hydrologic sources for seasonal signal for the wet season (dry season behaves in the opposite manner. **(a)** Elastic loading of the Great Valley causes extension (red vectors) at the surface and contraction (blue vectors) at depth. **(b)** Poroelastic loading of the Great Valley causes contraction at the surface and at depth. **(c)** Elastic loading of the region surrounding the San Andreas Fault. Question marks denote regions where we are uncertain regarding the earth response to the load. Particularly, we are not sure in (b) the depth of reach of the effect. In (c) we are unsure how wide the load is and whether to assume it is a point load or a distributed disk load.

analyzed M ≥ 6.4 mainshocks for California between 1850 and 2011. The author cited significant clustering of earthquake events in the spring and fall and attributed this to the timing of upward (dilatational) solar semiannual tides, rather than a seasonal trigger.

We hypothesize several potential hydrologic causes of the seasonal signal (Figure 15). First, a water load imposed on the Great Valley can cause the solid-Earth to respond elastically (Figure 15a), causing contraction at depth near the San Andreas Fault in the wet

season. At the surface in areas adjacent to the location of the load, this would cause GPS stations to move towards the Great Valley and away from the San Andreas Fault. However, this is not the general phenomenon observed by the GPS data in the wet season. Second, water entering the Great Valley sediments seasonally can behave poroelastically (Figure 15b), allowing expansion of the volume of sediments at depth in the Great Valley in the wet season. This would cause GPS stations to move towards the San Andreas Fault, leading to contraction at the surface as well as at depth. Although this is what we observe in the GPS displacements, at this point in time we are uncertain as to the depth of reach for this phenomenon and whether or not it can affect seismogenic depths. Finally, a water load imposed directly above the San Andreas Fault, an area that receives a large amount of rain in the wet season, could modulate the fault behavior (Figure 15c). However, a model of the distribution of surface and groundwater for this region is currently unavailable, so we are uncertain if the load behaves more as a distributed disk or as a point load. Each would cause different behavior both at the surface and at seismogenic depths. In addition, thermoelastic [e.g. *Prawirodirdjo et al.*, 2006; *Tsai,* 2011; *Ben-Zion and Allam*, 2013], tidal loading [e.g. *Métivier et al.,* 2009; *Delorey et. al.,* 2017], and atmospheric [e.g *vanDam et al.*, 1994] loading could be potential causes of the observed seasonal strain anomalies, but are not considered in detail at this point in time.

In relation to the potential correlation between groundwater pumping/recharge of the nearby Great Valley aquifer and strain, there is a strong correlation between peaks in contraction during the wet season (February/March) and in extension during the dry season (August/September) along the creeping section of the San Andreas Fault. Several studies using data from the GRACE satellites show general seasonal trends of high equivalent

water heights in the wet season and low equivalent water heights in the dry season [*Scanlon et. al.,* 2012; *Famiglietti and Rodell,* 2013]. These observations are for the entire Great Valley, as GRACE lacks the spatial resolution to distinguish between the seasonal signals in the basin adjacent to the locked and creeping San Andreas Fault. Well data from the USGS adjacent to the creeping section do show considerable seasonality aligning with the horizontal observations of the GPS data in the creeping section (high water levels in the wet period contrasting with low water levels in the dry period).

Due to large reference evapotranspiration rates (up to 140cm/year) [*Faunt,* 2009] in the southern Great Valley from high summer temperatures (often exceeding 100^{o}F/38^{o}C) [*Durrenberger,* 1965], the Southern Great Valley sees the highest pumping rates. It is, therefore, expected that the locked section would show considerable seasonality. However, with the exception of the month of June near the eastward bend of the San Andreas Fault, the locked section (south of Cholame) shows little seasonality. Hydrograph models simulating water-level altitudes generally suggest larger seasonal fluctuations (up to 50 meters additional annual change in water level) here in comparison to where the Great Valley aligns with the creeping section [*Faunt,* 2009, Figure B13]. However, since actual continuous well-water data only exists for the time period of interest where the Great Valley parallels the creeping section, it can't necessarily be argued that the model presented in *Faunt* [2009] is relevant to our conclusions. In future, we need to create a joint model of all situations presented in Figure 15, which includes considerations of geology, the interplay between the confined and unconfined aquifers of the Great Valley, well water, and InSAR subsidence rates to fully explore this phenomenon.

A strong contrast in the magnitude of seasonality of strain between the creeping and locked sections of the San Andreas Fault suggests that factors other than hydrology may influence the seasonal GPS signal. One of the most prevalent distinctions between the creeping and locked sections lies in the differences in fault strength and bedrock geology. The creeping section, in comparison to the locked section, is inherently weak ($\mu \sim 0.1$ to 0.15) due to the saponite existing at seismogenic depths from a unique reaction of mg-rich serpentine with quartzofeldspathic rocks from the Great Valley Sequence [*Lockner,* 2011; *Moore and Lockner,* 2013; *Carpenter et al.,* 2015]. However, borehole core from the locked section demonstrates a far larger coefficient of friction, similar to that of the surrounding crust [e.g. *McGarr et al.,* 1982]. This suggests that the weaker, creeping section may be more prone to influences by external forces than the stronger, locked section.

Other factors which could be influencing the lack of seasonality in the locked section are (1) less GPS coverage in the locked section giving a lower resolution signal and (2) the distance between the Great Valley and the San Andreas Fault. For (1), further analysis that combines datasets such as InSAR and borehole strain meters would help clarify the near-fault seasonal signal in the locked section at a higher resolution. In terms of (2), the distance between the Great Valley and the San Andreas Fault is shorter adjacent to the locked section in comparison to the creeping section. Depending on the size of the load, the ideal distance to give a peak seasonality along the San Andreas Fault may be neighboring to the creeping section, rather than the locked section.

5

Conclusions

The results presented in this work suggest a correlation between seasonal (un-)loading of fault structures in the study region, seasonality, and water storage patterns. A robust seasonal model of dilatational and shear strain for Central California is presented and generally correlates with previous works that suggest a seasonal variation of seismicity. The seasonal strain model shows spatially coherent patterns of peak extensional strain in the dry season (August/September) and peak contractional strain in the wet season (February/March) along the main creeping section of the San Andreas Fault. In the preferred model, the north transitional creeping section of the San Andreas Fault and the Calaveras Fault also show general similarities with the patterns observed in the main creeping section. In sharp contrast, seasonality is virtually undetectable in the locked section of the San Andreas Fault (south of Cholame). Additionally, the southern transitional creeping section shows two distinct patterns. For the most part this region, between Parkfield and Cholame, shows seasonal strain patterns similar to the main creeping section. However, the segment of the southern transitional creeping section surrounding the town of Cholame opposes this trend with peaks in extension during the wet period and peaks in contraction during the dry period.

Several hydrologic causes for the seasonal signal in the creeping section are postulated. Possible reasoning for a null result along the locked section of the San Andreas Fault is hypothesized to be associated with (1) reduced resolution of the strain model in the locked section due to reduced GPS station coverage, (2) a difference in frictional strength coming from a variation in geologic properties of the locked section in comparison to the main creeping section, or (3) difference in distance between the San Andreas Fault and Great Valley. We plan to explore these causes and reasoning further in future work.

References

Alpert (1986), Mesoscale Indexing of the Distribution of Orographic Precipitation over High Mountains, *J. Clim. Appl. Meteorol.,* v. 25, 532 – 545, doi: 10.1175/1520-0450(1986)025<0532:MIOTDO>2.0.CO;2

Allen, C. R. (1968), The tectonic environments of seismically active and inactive areas along the San Andreas fault system, in *Proceedings of Conference on Geologic Problems of San Andreas Fault System*, edited by W. R. Dickinson and A. Grantz, pp. 70 – 82, Stanford University Geological Publications, v. 11, Stanford, C.A.

Amos, C. B., P. Audet, W. C. Hammond, R. Bürgmann, I. A. Johanson, and G. Blewitt (2014), Uplift and seismicity driven by groundwater depletion in central California, *Nature*, v. 509, 483-486, doi:10.1038/nature13275.

Argus, D. F. and R. G. Gordon (2001), Present tectonic motion across the Coast Ranges and San Andreas fault system in central California, *GSA Bull.,* v. 113 (12), 1580-1592, doi: 10.1130/0016-7606(2001)113<1580:PTMATC>2.0.CO;2.

Argus, D. F., M. B. Heflin, G. Peltzer, F. Crampé, and F. H. Webb (2005), Interseismic strain accumulation and anthropogenic motion in metropolitan Los Angeles, *J. Geophys. Res*., v. 110, B04401, doi:10.1029/2003JB002934.

Argus, D. F., Y. Fu, and F. W. Landerer (2014), Seasonal variation in total water storage in California inferred from GPS observations of vertical land motion, *Geophys. Res. Lett.*, v. 41, doi:10.1002/ 2014GL059570.

Atwater, T. (1970), Implications of plate tectonics for the cenozoic tectonic evolution of western North America, *GSA Bull.,* v. 81, 3513-3536, doi: 10.1130/0016-7606(1970)81[3513:IOPTFT]2.0.CO;2.

Atwater, T. and J. Stock (1998), Pacific-North America plate tectonics of the neogene southwestern United States - An Update, *Int. Geology Rev.,* v. 40, 375 – 402, doi: 10.1080/00206819809465216.

Baxter, S. C., S. Kedar, J. W. Parker, F. H. Webb, S. E. Owen, A. Sibthorpe, and D. Dong (2011), Limitations of strain estimation techniques from discrete deformation observations, *Geophys. Res. Lett.*, v. 38, L01305, doi:10.1029/2010GL046028.

Ben-Zion, Y. and Allam, A.A. (2013), Seasonal thermoelastic strain and postseismic effects in Parkfield borehole dilatometers. *Earth & Planet. Sci. Lett*., v. 379, 120–126. doi: 10.1016/j.epsl.2013.08.024.

Bennett, R. A., B. P. Wernicke, N. A. Niemi, A. M. Friedrich, and J. L. Davis (2003), Contemporary strain rates in the northern Basin and Range province from GPS data, *Tectonics*, v. 22, 1008, doi:10.1029/2001TC001355.

Bergmann, I., G. Ramillien, and F. Frappart, (2012), Climate-driven interannual ice mass evolution in Greenland. *Global and Planetary Change*, v. 82–83, 1-11, doi: 10.1016/j.gloplacha.2011.11.005.

Bittman, M. (2012) Everyone eats there, *NY Times Magazine,* (New York, NY), Oct. 10, 2012, http://www.nytimes.com/2012/10/14/magazine/californias-central-valley-land-of-a-billion-vegetables.html, last accessed March 27, 2017.

Blake M. C. and D. L. Jones (1981), The Franciscan assemblage and related rocks in northern California: a reinterpretation, in *The Geotectonic Development of California, Rubey Volume I*, edited by W. G. Ernst, pp. 307 – 328, Prentice-Hall, Inc., Englewood Cliffs, N.J.

Blewitt, G., C. Kreemer, W.C. Hammond, and J.M. Goldfarb, (2013), Terrestrial reference frame NA12 for crustal deformation studies in North America. *Journal of Geodynamics* v. 72, 11 – 24, doi:10.1016/j.jog.2013.08.004.

Blewitt, G., C. Kreemer, W. C. Hammond, and J. Gazeaux (2016), MIDAS robust trend estimator for accurate GPS station velocities without step detection. *J. Geophys. Res.*, v. 121, doi:10.1002/2015JB012552.

Borsa, A. A., D. C. Agnew, and D. R. Cayan (2014), Ongoing drought-induced uplift in the western United States, *Science,* v. 345, 1587-1590, doi: 10.1126/science.1260279.

Burford, R. O. and P. W. Harsh (1980), Slip on the San Andreas Fault in central California from alinement array surveys, *Bull. Seismol. Soc. Amer.*, v. 70 (4), 1233 – 1261.

California Department of Water Resources (2003), Bulletin 118: Groundwater Basin Maps and Descriptions, accessed 7/15/2015, Dataset, URL: http://www.water.ca.gov/groundwater/bulletin118/gwbasins.cfm and https://gis.water.ca.gov/app/groundwater/.

California Department of Water Resources Data Library (2015), Spring Groundwater Level Change Maps, Groundwater Information Center, accessed 4/8/2017, Dataset, URL: www.water.ca.gov/groundwater/maps_and_reports/index.cfm

Carle, D. (2016), *Introduction to Water in California*, The Regents of the University of California, Oakland, C.A.

Carpenter, B. M., D. M. Saffer, and C. Marone (2015), Frictional properties of the active San Andreas Fault at SAFOD: Implications for fault strength and slip behavior, *J. Geophys. Res.*, v. 120, 5273–5289, doi:10.1002/ 2015JB011963.

Chaussard, E., R. Bürgmann, M. Shirzaei, E. J. Fielding, and B. Baker (2014), Predictability of hydraulic head changes and characterization of aquifer-system and fault properties from InSAR-derived ground deformation, *J. Geophys. Res.*, v. 119, 6572–6590, doi:10.1002/ 2014JB011266.

Christiansen, L. B., S. Hurwitz, and S. E. Ingebritsen (2007), Annual modulation of seismicity along the San Andreas Fault near Parkfield, C.A., *Geophys. Res. Lett*., v. 34, L04306, doi:10.1029/2006GL028634.

Cleveland, R. B., W. S. Cleveland, J. E. McRae, and I. Terpenning (1990), STL: A seasonal-trend decomposition procedure based on loess. *J. of Official Statistics*, v. 6 (2), 3 – 33.

Davis, J. L., B. P. Wernicke, and M. E. Tamisiea (2012), On seasonal signals in geodetic time series, *J. Geophys. Res.*, v. 117, B01403, doi:10.1029/2011JB008690.

deBoor, C. (1978), *A Practical Guide to Splines*, Springer-Verlag, New York.

Delaunay, B. (1934), Sur la sphère vide, Bull. Acad. Sci. USSR, v. 7, 793–800.

Delorey, A. A., N. J. van der Elst, and P. A. Johnson (2017), Tidal triggering of earthquakes suggests poroelastic behavior on the San Andreas Fault, *Earth & Planet. Sci. Lett.,* v. 460, 164 – 170, doi: 10.1016/j.epsl.2016.12.014

DeMets, C. and Dixon, T. H. (1999), New kinematic models for Pacific-North America motion from 3 Ma to present, I: Evidence for steady motion and biases in the NUVEL-1A Model, *Geophys. Res. Lett.,* v. 26 (13), 1921 – 1924, doi: 10.1029/1999GL900405.

Dickinson, W. R. (1981), Plate Tectonics and the continental margin of California, in *The Geotectonic Development of California, Rubey,* v. I, edited by W. G. Ernst, pp. 1 – 28, Prentice-Hall, Inc., Englewood Cliffs, N.J.

Dixon, T. H., M. Miller, F. Farina, H. Wang, and D. Johnson (2000), Present-day motion of the Sierra Nevada block and some tectonic implications for the Basin and Range province, North American Cordillera, *Tectonics*, v. 19(1), 1–24, doi:10.1029/1998TC001088.

Durrenberger (1965), *Patterns on the land*, 3rd edition, National Press Books, Palo Alto, C.A.

Dutilleul, P., C. W. Johnson, R. Bürgmann, Y. Wan, and Z.-K. Shen (2015), Multifrequential periodogram analysis of earthquake occurrence: An alternative approach to the Schuster spectrum, with two examples in central California, *J. Geophys. Res.*, v. 120, 8494–8515, doi:10.1002/2015JB012467.

Famiglietti, J. S. and M. Rodell (2013), Water in Balance, *Science,* v. 340, 1300 – 1301, doi: 10.1126/science.1236460

Faunt, C. C. ed. (2009), Groundwater availability of the Central Valley Aquifer, California, *U.S. Geological Survey Professional Paper 1766*, 225 p.

Faunt, C. C. and Sneed, M. (2015), Water availability and subsidence in California's Central Valley, *San Francisco Estuary and Watershed Science,* v. 13 (3), art. 4, doi: 10.15447/sfews.v13iss3art4

Farr, T. G., C. E. Jones, and Z. Liu (2016), Progress Report: Subsidence in California, March 2015 – September 2016, *Jet Propulsion Laboratory*, Pasadena, C.A.

Farrar, C. D. and G. L. Bertoldi (1988), Region 4, Central Valley and Pacific Coast Ranges, in *Hydrogeology, The Geology of North America*, edited by W. Back, J. S. Rosenshein, and P. R. Seaber, pp. 59 – 67, The Geological Society of America, Boulder, C.O.

Fliedner, M. M., S. L. Klemperer, and N. I. Christensen (2000), Three-dimensional seismic model of the Sierra Nevada arc, California, and its implications for crustal and upper mantle composition, *J. Geophys. Res.*, v. 105(B5), 10899–10921, doi:10.1029/2000JB900029.

Galehouse, J. S. and J. J. Lienkaemper (2003), Inferences drawn from two decades of alinement array measurements of creep on faults in the San Francisco Bay Region, *Bull. Seismol. Soc. Amer,* v. 93 (6), 2415 – 2433, doi: 10.1785/0120020226.

Hackl, M., R. Malservisi, and S. Wdowinski (2009), Strain rate patterns from dense GPS networks, *Nat. Hazards Earth Syst. Sci*, v.9, 1177-1187, doi:10.5194/nhess-9-1177-2009.

Haines, A. J., and W. E. Holt (1993), A procedure for obtaining the complete horizontal motions within zones of distributed deformation from the inversion of strain rate data, *J. Geophys. Res*., v. 98(B7), 12057–12082, doi:10.1029/93JB00892.

Haines, A. J., J. A. Jackson, W. E. Holt, and D. C. Agnew (1998), Representing distributed deformation by continuous velocity fields, *Sci. Rept. 98/5, Inst. Of Geol. and Nucl. Sci.,* Wellington, New Zealand.

Hammond, W. C., G. Blewitt, and C. Kreemer (2016), GPS Imaging of vertical land motion in California and Nevada: Implications for Sierra Nevada uplift, *J. Geophys. Res.*, v. 121, doi:10.1002/2016JB013458.

Hardebeck, J. L., J. Boatwright, D. Dreger, R. Goel, V. Graizer, K. Hudnut, C. Ji, L. Jones, J. Langbein, J. Lin, E. Roeloffs, R. Simpson, K. Stark, R. Stein, and J. C. Tinsley (2004), Preliminary report on the 22 December 2003, M 6.5 San Simeon, California Earthquake, *Seismol. Res. Lett.,* v. 75 (2), 155 – 172, doi: 10.1785/gssrl.75.2.155.

Harris, R. A., and P. Segall (1987), Detection of a locked zone at depth on the Parkfield, California, segment of the San Andreas Fault, *J. Geophys. Res.*, v. 92(B8), 7945–7962, doi:10.1029/JB092iB08p07945.,

Heki, K. (2001), Seasonal modulation of interseismic strain buildup in northeastern Japan driven by snow loads, *Science*, v. 293, 89 – 92, doi: 10.1126/science.1061056

Heki, K. (2003), Snow load and seasonal variation of earthquake occurrence in Japan, *Earth & Planet. Sci. Lett*., v. 207, 159 – 164, doi: 10.1016/S0012-821X(02)01148-2.

Hill, D. P., J. P. Eaton, and L. M. Jones (1990), Seismicity 1980 – 86, in *The San Andreas Fault System, California, U.S. Geological Survey Professional Paper 1515,* edited by R. E. Wallace, pp. 115 – 151., U.S. Government Printing Office, Washington, D.C.

Holt, W. E., B. Shen-Tu, J. Haines, and J. Jackson (2000), On the determination of self-consistent strain rate fields within zones of distributed deformation, in *The History and Dynamics of Global Plate Motions, Geophys. Monogr. Ser.,* vol. 121, edited by M. A. Richards, R. G. Gordon, and R. D. van der Hilst, pp. 113 – 141, American Geophysical Union, Washington, D. C.

Humphreys, E., E. Hessler, K. Dueker, G. L. Farmer, E. Erslev and T. Atwater (2003), How Laramide – age hydration of North American lithosphere by the Farallon Slab controlled subsequent activity in the Western United States.

Irwin, W. P., and I. Barnes (1975), Effect of geologic structure and metamorphic fluids on seismic behavior of the San Andreas fault system in central and northern California, *Geology*, v. 3(12), 713–716, doi:10.1130/0091-7613(1975)3<713:EOGSAM>2.0.CO;2.

Ji, K. H., and T. A. Herring (2012), Correlation between changes in groundwater levels and surface deformation from GPS measurements in the San Gabriel Valley, California, *Geophys. Res. Lett.*, v. 39, L01301, doi:10.1029/2011GL050195.

Jin, S., D. P. Chambers, and B. D. Tapley (2010), Hydrological and oceanic effects on polar motion from GRACE and models, *J. Geophys. Res*., v. 115, B02403, doi:10.1029/2009JB006635.

Kreemer, C., W. C. Hammond, G. Blewitt, A. A. Holland, and R. A. Bennett (2012), A geodetic strain rate model for the Pacific – North American plate boundary, western United States, *Map 178*, scale 1:1,500,000, Nevada Geodetic Laboratory, Nevada Bureau of Mines and Geology, Reno, NV.

Krige, D. G. (1951), A statistical approach to some mine valuations and allied problems at the Witwatersrand, M.S. thesis, Univ. of Witwatersrand, Johannesburg, South Africa.

Langbein, J. (2004), Noise in two-color electronic distance meter measurements revisited, *J. Geophys. Res*., v. 109, B04406, doi:10.1029/2003JB002819.

Lafare, A. E. A., D. W. Peach, A. G. Hughes (2016), Use of seasonal trend decomposition to understand groundwater behaviour in the Permo-Triassic Sandstone aquifer, Eden Valley, UK. *Hydrogeology Journal*, v. 24 (1), 141 – 158, doi: 10.1007/s10040-015-1309-3.

Lisowski, M. and W. H. Prescott (1981), Short-range distance measurements along the San Andreas Fault system in central California, 1975 to 1979, *Bull. Seismol. Soc. Amer.*, v. 71 (5), 1607 – 1624.

Lockner, D. A., C. Morrow, D. Moore, and S. Hickman (2011), Low strength of deep San Andreas Fault gouge from SAFOD core, *Nature*, v. 472, 82–85, doi:10.1038/nature09927.

Matheron, G. (1963), Principals of geostatistics, *Econ. Geol.*, v. 58(8), 1246–1266, doi:10.2113/gsecongeo.58.8.1246.

McCaffrey, R. (2005), Block kinematics of the Pacific–North America plate boundary in the southwestern United States from inversion of GPS, seismological, and geologic data, *J. Geophys. Res*., v. 110, B07401, doi:10.1029/2004JB003307.

McGarr, A., M. D. Zoback, and T. C. Hanks (1982), Implications of an elastic analysis of in situ stress measurements near the San Andreas Fault, *J. Geophys. Res*., v. 87(B9), 7797–7806, doi:10.1029/JB087iB09p07797.

McLaren, M. K. and W. U. Savage (2001) Seismicity of south-central coastal California: October 1987 through January 1997, *Bull. Seismol. Soc. Amer.*, v. 91 (6), 1629 – 1658, doi: 10.1785/0119980192.

Métivier, L., O. de Viron, C. P. Conrad, S. Renault, M. Diament, and G. Patau (2009), Evidence of earthquake triggering by the solid earth tides, *Earth Planet. Sci. Lett.*, v. 278(3–4), 370–375, doi:10.1016/j.epsl.2008.12.024.

Moore, D. E., and D. A. Lockner (2013), Chemical controls on fault behavior: Weakening of serpentinite sheared against quartz-bearing rocks and its significance for fault creep in the San Andreas system, *J. Geophys. Res.*, v. 118, 2558–2570, doi:10.1002/jgrb.50140.

Nadeau, R. M., W. Foxall, and T. V. McEvilly (1995), Clustering and periodic recurrence of microearthquakes on the San Andreas Fault at Parkfield, California, *Science,* v. 267 (5197), 503 – 507, doi: 10.1126/science.267.5197.503.

Nadeau, R. M. and D. Dolenc (2005), Nonvolcanic tremors deep beneath the San Andreas Fault, *Science,* v. 307 (5708), 389, doi: 10.1126/science.1107142.

Nadeau, R. M. and A. Guilhem (2009), Nonvolcanic Tremor Evolution and the San Simeon and Parkfield, California, Earthquakes, *Science*, v. 325 (5937), 191-193, doi: 10.1126/science.1174155.

Nevada Geodetic Laboratory (2016), GPS Time Series Master Steps Database, University of Nevada, Reno, Dataset, accessed 8/15/2016, URL: http://geodesy.unr.edu/NGLStationPages/steps.txt.

NCEDC (2014), Northern California Earthquake Data Center. UC Berkeley Seismological Laboratory. Dataset. doi:10.7932/NCEDC.

Page, B. M. (1981), The Southern Coast Ranges, in *The Geotectonic Development of California, Rubey,* v. I, edited by W. G. Ernst, pp. 329 – 417, Prentice-Hall, Inc., Englewood Cliffs, N.J.

Page, B. M., G. A. Thompson, R. G. Coleman (1998), OVERVIEW: Late Cenozoic tectonics of the central and southern Coast Ranges of California, *GSA Bull.*, v. 110 (7), 846 – 876, doi:10.1130/0016-7606(1998)110<0846:OLCTOT>2.3.CO;2.

Pandey, G. R., D. R. Cayan, and K. P. Georgakakos (1999) Precipitation structure in the Sierra Nevada of California during winter, *J. Geophys. Res.,* v. 104 (D10), 12019-12030, doi:10.1029/1999JD900103.

Planert, M. and Williams, J. S. (1995), Segment 1: California and Nevada, in *Ground Water Atlas of the United States*, *Hydrologic Investigations Atlas,* 730-B, edited by James A. Miller, U. S. Geological Survey, Reston, VA.

Prawirodirdjo, L., Ben-Zion, Y., and Bock, Y., (2006). Observation and modeling of thermoelastic strain in Southern California Integrated GPS Network daily position time series, *J. Geophys. Res.*, v. 111, B02408, doi:10.1029/2005JB003716.

Provost, A.-S., and H. Houston (2003), Stress orientations in northern and central California: Evidence for the evolution of frictional strength along the San Andreas plate boundary system, *J. Geophys. Res*., v. 108 (B3), 2175, doi:10.1029/2001JB001123.

Reid, H. F. (1910) The Mechanics of the Earthquake, The California Earthquake of April 18, 1906, *Report of the State Investigation Commission*, v. 2, Carnegie Institution of Washington, Washington, D.C.

Renka, R. J. (1997), Algorithm 772: STRIPACK: Delaunay triangulation and Voronoi diagram on the surface of a sphere, *ACM Trans. Math. Soft.*, v. 23(3), 416–434.

Rice, J. R. (1992), Fault Stress States, Pore Pressure Distributions, and the Weakness of the San Andreas Fault, in *Fault Mechanics and Transport Properties of Rocks, International Geophysics Series,* vol. 51, edited by Brian Evans and Teng-Fong Wong, pp. 475 – 517, Academic Press Inc., San Diego, CA.

Roeloffs, E. A. (2001), Creep rate changes at Parkfield, California 1966–1999: Seasonal, precipitation induced, and tectonic, *J. Geophys. Res*., v. 106(B8), 16525–16547, doi:10.1029/2001JB000352.

Rymer, M. J. and W. L. Ellsworth (1983), The Coalinga, California, earthquake of May 2, 1983, *U.S. Geological Survey Professional Paper 1487*, 417 p., U.S. Government Printing Office, Washington, D.C.

Savage, J. C. and R. O. Burford (1973), Geodetic determination of relative plate motion in central California, *J. Geophys. Res.,* v. 78 (5), 832 – 845, doi: 10.1029/JB078i005p00832.

Scanlon, B. R., C. C. Faunt, L. Longuevergne, R. C. Reedy, W. M. Alley, V. L. McGuire, and P. B. McMahon (2012), Groundwater depletion and sustainability of irrigation in the US High Plains and Central Valley, *PNAS*, v. 109 (24), 9320–9325, doi: 10.1073/pnas.1200311109.

Scanlon, B. R., L. Longuevergne, and D. Long (2012), Ground referencing GRACE satellite estimates of groundwater storage changes in the California Central Valley, USA, *Water Resour. Res.*, v. 48, W04520, doi:10.1029/2011WR011312.

Schmalzle, G., T. Dixon, R. Malservisi, and R. Govers (2006), Strain accumulation across the Carrizo segment of the San Andreas Fault, California: Impact of laterally varying crustal properties, *J. Geophys. Res.*, v. 111, B05403, doi:10.1029/2005JB003843.

Schulz, S. S., G. M. Mavko, R. O. Burford, and W. D. Stuart (1982), Long-term fault creep observations in central California, *J. Geophys. Res.,* v. 87(B8), 6977–6982, doi:10.1029/JB087iB08p06977.

Scholz, C. H. (2002), *The Mechanics of Earthquakes and Faulting*, 2nd edition, Cambridge University Press, Cambridge, UK.

Scholz, C. H. (2006), The Strength of the San Andreas Fault: A Critical Analysis, in *Earthquakes Radiated Energy and the Physics of Faulting, Geophys. Monogr. Ser.,* vol. 170, edited by Rachel Abercrombie, Art McGarr, Giulio DiToro, Hiroo Kanamori, pp. 301 – 311, AGU, Washington, DC.

Schorlemmer, D. and S. Wiemer (2005), Microseismicity data forecast rupture area, *Nature,* v. 434, 1086, doi:10.1038/4341086a

Sieh (1978), Slip along the San Andreas Fault associated with the great 1857 earthquake, *Bull. Seismol. Soc. Amer.*, v. 68 (5), 1421 – 1448.

Silverii, F., N. D'Agostino, M. Métois, F. Fiorillo, and G. Ventafridda (2016), Transient deformation of karst aquifers due to seasonal and multiyear groundwater variations observed by GPS in southern Apennines (Italy), J. Geophys. Res., v. 121, 8315–8337 doi:10.1002/2016JB013361.

Thatcher (1975), Strain accumulation and release mechanism of the 1906 San Francisco earthquake, *J. Geophys. Res.*, v. 80 (35), 4862 – 4872, doi: 10.1029/JB080i035p04862.

Titus, S. J., C. DeMets, and B. Tikoff (2005), New slip rate estimates for the creeping segment of the San Andreas Fault, California, *Geology*, v. 33 (3), 205 – 208, doi: 10.1130/G21107.1.

Titus, S. J., M. Dyson, C. DeMets, B. Tikoff, F. Rolandone, and R. Bürgmann (2011a), Geologic versus geodetic deformation adjacent to the San Andreas Fault, central California, *GSA Bull.*, v. 123 (5/6), 794 – 820, doi: 10.1130/B30150.1.

Titus, S. J., S. Crump, Z. McGuire, E. Horsman, and B. Housen (2011b), Using vertical axis rotations to characterize off-fault deformation across the San Andreas Fault system, central California, *Geology*, v. 39 (8), 711 – 714, doi: 10.1130/G31802.1.

Tsai, V. C. (2011), A model for seasonal changes in GPS positions and seismic wave speeds due to thermoelastic and hydrologic variations, *J. Geophys. Res.*, v. 116, B04404, doi:10.1029/2010JB008156.

U.S. Geological Survey and California Geological Survey (2006), Quaternary fault and fold database for the United States, accessed 1/1/2010, Dataset, URL: http//earthquakes.usgs.gov/hazards/qfaults/.

U.S.D.A. Census of Agriculture – State Data (2012), Market value of agriculture products, State of California, accessed 3/20/2017, https://www.agcensus.usda.gov/Publications/2012/Full_Report/Volume_1,_Chapter_1_State_Level/California/st06_1_002_002.pdf

vanDam, T. M., G. Blewitt, and M. B. Heflin (1994), Atmospheric pressure loading effects on Global Positioning System coordinate determinations, *J. Geophys. Res. Solid Earth*, v. 99(B12), 23939–23950, doi:10.1029/94JB02122.

Wesnousky (2005), The San Andreas and Walker Lane fault systems, western North America: transpression, transtension, cumulative slip and the structural evolution of a major transform boundary, *J. Struct. Geol.,* v. 27 (8), 1505 – 1512, doi: 10.1016/j.jsg.2005.01.015

Wesnousky (2006), Predicting the endpoints of earthquake ruptures, *Nature,* v. 444, 358 – 360, doi: 10.1038/nature05275

Wessel, P., and W. H. F. Smith (1998), New, improved version of generic mapping tools released, *Eos Trans. AGU*, v. 79(47), 579–579, doi:10.1029/98EO00426.

Wessel, P., W. H. F. Smith, R. Scharroo, J. Luis and F. Wobbe (2013), Generic Mapping Tools: Improved Version Released, *Eos Trans*. *AGU*, v. 94(45), 409.

Wesson, R. L., R. O. Burford, and W. L. Ellsworth (1973), Relationship between seismicity, fault creep and crustal loading along the central San Andreas Fault, in *Proceedings of Conference on Tectonic Problems of San Andreas Fault System,* edited by R. L. Kovach and A. Nur, pp. 303 – 321, Stanford University Geological Publications, v. 13, Stanford, C.A.

Zoback, M. D., S. Hickman, and W. Ellsworth (2010), Scientific Drilling Into the San Andreas Fault Zone, *Eos Trans. AGU*, v. 91(22), 197–199, doi:10.1029/2010EO220001.

Zoback, M. D., S. Hickman, W. Ellsworth, and the SAFOD Science Team (2011), Scientific drilling into the San Andreas Fault Zone—An overview of SAFOD's first five years, *Sci. Drill.*, no. 11, 14–28, doi:10.2204/iodp.sd.11.02.2011

Appendix

Table A1 Stations included for the analysis are ordered alphabetically by name with their associated before and during drought rates. Those listed as "NO RATE" mean that the MIDAS preliminary criteria to generate a rate was not met (mostly) due to a very limited amount of data in the GPS time series.

	Station Name	Longitude	Latitude	Before Drought Vertical Rate	During Drought Vertical Rate
1	BBDM	240.01849	34.58220	1.283	-2.265
2	BCWR	240.59415	34.92046	0.41	1.428
3	BEPK	241.92591	35.87839	-0.562	0.931
4	BRPK	241.42319	34.68228	0.445	0.896
5	BVPP	240.65249	35.15728	-1.479	1.769
6	CAHB	237.50965	37.50617	NO RATE	-0.834
7	CAMT	238.17975	36.57962	NO RATE	0.922
8	CAND	239.56630	35.93935	1.111	2.632
9	CARH	239.56918	35.88838	1.487	-0.524
10	CASN	240.15471	34.41569	NO RATE	0.783
11	CASZ	237.94539	36.95896	NO RATE	-0.252
12	CCCC	242.32883	35.56531	-1.396	0.085
13	CCST	240.98654	34.80636	-0.066	2.082
14	CMBB	239.61396	38.03418	-2.247	0.500
15	COPR	240.12048	34.41491	-1.099	0.376
16	CRBT	239.24925	35.79161	0.058	1.298
17	CRU1	240.21519	34.02926	-0.318	-0.122
18	CSST	240.62875	34.40809	-0.431	-0.868
19	DAPK	239.22849	35.25427	-1.415	-0.619
20	DCAN	239.15491	35.21152	1.355	1.038
21	DIAB	238.08437	37.87858	-0.229	-0.631
22	DOND	240.30988	37.26425	NO RATE	4.180
23	EDPP	241.16959	34.94619	0.724	2.175
24	ELTN	241.57427	34.70312	NO RATE	0.612
25	FGST	239.99062	34.73301	0.569	1.474
26	FMTP	241.10586	34.40986	-0.951	-3.331
27	GDEC	240.13632	35.18941	0.35	2.198
28	GR8R	239.58427	36.39902	0.697	1.335
29	HELB	240.97703	36.67884	NO RATE	0.170
30	HOGS	239.52050	35.86671	0.284	2.039
31	HUNT	239.59762	35.88081	0.348	2.614
32	HVYS	240.81246	34.44123	-1.081	-0.671
33	ISLK	241.52570	35.66227	-0.672	2.685

34	JLN5	239.16710	35.87317	NO RATE	0.441
35	JRSC	237.77260	37.40625	NO RATE	-0.861
36	KBRC	240.99180	34.39853	-0.32	-1.802
37	LAND	239.52672	35.89979	-0.075	1.787
38	LJRN	241.13226	34.80752	4.217	2.062
39	LOWS	239.40572	35.82871	0.318	1.732
40	LUTZ	238.13478	37.28685	-2.598	0.185
41	LVMS	240.89632	34.73360	0.309	2.291
42	MASW	239.55694	35.83260	-0.028	2.489
43	MEE1	239.24140	36.18690	1.377	3.040
44	MEE2	239.23315	36.18052	0.406	3.123
45	MHCB	238.35742	37.34153	1.252	0.730
46	MIG1	239.64861	34.03826	-0.324	-0.479
47	MILP	238.16592	37.44904	NO RATE	-0.898
48	MNMC	239.56595	35.96947	0.848	2.935
49	MUSB	240.69065	37.16994	-0.775	1.674
50	NHRG	240.85874	34.49866	-0.51	0.854
51	OVLS	240.85805	34.32736	-0.233	-1.474
52	OXMT	237.57568	37.49936	-6.14	3.976
53	OZST	240.64659	34.68337	1.389	1.738
54	P067	238.99704	35.55175	-1.115	1.404
55	P171	238.20748	36.48552	-0.331	-1.523
56	P172	238.23276	36.22807	-0.424	-1.365
57	P173	238.70967	35.94572	-0.673	0.635
58	P174	238.94910	36.30215	-0.202	2.241
59	P175	238.86514	36.42590	-0.04	2.111
60	P176	237.64286	37.47177	-0.46	-1.471
61	P177	237.50495	37.52817	-1.172	-1.192
62	P178	237.66764	37.53452	-3.282	-0.933
63	P180	238.59676	36.29283	-0.192	0.440
64	P209	237.87329	37.06925	-0.226	-0.081
65	P210	238.26816	36.81614	-0.48	-0.623
66	P211	238.30196	36.87918	-0.073	0.738
67	P212	238.13727	36.96201	-0.88	0.140
68	P213	238.00916	37.20171	-1.247	-0.719
69	P214	238.20343	37.00102	-0.737	1.280
70	P215	238.23705	37.04878	-2.316	0.135
71	P216	238.27379	37.00243	-0.112	-0.369
72	P217	238.34937	37.10450	3.028	-0.581
73	P218	238.28604	37.20351	-1.501	0.125
74	P219	237.71518	37.34249	0.654	-1.003
75	P220	237.78572	37.32989	-0.672	-0.826
76	P221	237.90095	37.33695	-1.173	-0.087

77	P222	237.91674	37.53924	-0.52	1.236
78	P223	237.90022	37.72205	-1.116	-0.527
79	P225	237.94167	37.71387	-1.061	-0.335
80	P226	238.17442	37.33678	1.203	-4.382
81	P227	238.21040	37.53297	-0.726	0.567
82	P228	238.31306	37.60184	-0.479	0.356
83	P229	238.02204	37.74943	-0.909	-0.827
84	P230	238.21360	37.81896	0.194	0.075
85	P231	238.09459	36.62168	-1.461	-0.064
86	P232	238.42096	36.72402	-0.607	0.732
87	P233	238.57972	36.80043	-1.529	-0.107
88	P234	238.40878	36.85853	-0.052	0.998
89	P235	238.45846	36.81427	0.17	0.402
90	P236	238.44554	36.90354	-0.583	1.073
91	P237	238.61317	36.63702	0.321	1.166
92	P238	238.54723	36.84908	-0.548	-2.491
93	P239	238.45221	36.96246	1.133	-0.691
94	P240	238.45797	37.00781	0.572	-2.010
95	P241	238.42574	37.21301	-0.668	0.294
96	P243	238.66485	36.91819	-0.611	1.558
97	P244	238.64548	37.01082	-1.162	0.725
98	P247	238.81157	36.55952	-0.016	2.318
99	P249	238.93559	36.61164	0.285	1.571
100	P250	238.73156	36.95004	-0.843	2.030
101	P251	238.65205	36.81145	0.696	1.972
102	P252	238.94227	37.16956	-1.527	2.014
103	P253	238.34699	37.47845	0.228	0.793
104	P254	238.53080	37.48963	-0.692	0.536
105	P255	238.67515	37.58188	-1.034	0.683
106	P256	238.39516	37.93196	-0.869	0.526
107	P257	238.53597	37.75529	1.028	-1.467
108	P258	238.71673	37.38539	-1.359	1.045
109	P275	238.78541	38.32153	-3.858	-2.313
110	P277	237.63312	37.19237	-0.835	-0.794
111	P278	238.93925	35.71125	1.529	2.002
112	P279	238.93798	35.79065	-0.304	1.653
113	P280	239.65240	35.54405	0.311	1.418
114	P281	239.61054	35.84106	-0.963	1.395
115	P282	239.65479	35.83781	0.77	3.132
116	P283	239.71474	35.80667	0.568	2.822
117	P284	239.09316	35.93326	0.048	0.268
118	P285	239.01852	36.41718	0.06	2.694
119	P286	239.14694	36.51591	-0.352	1.306

120	P287	239.30217	36.02483	0.123	0.700
121	P288	239.12110	36.14021	-0.585	1.963
122	P289	239.25118	36.10684	0.125	2.060
123	P290	239.27175	36.17894	0.568	2.266
124	P291	239.35523	35.92278	-0.526	1.800
125	P292	239.52472	36.00746	1.161	2.839
126	P293	239.45701	36.08936	0.375	2.764
127	P294	239.56012	36.12324	0.29	3.093
128	P295	239.15762	35.69708	0.786	2.012
129	P296	239.63644	36.05165	0.808	2.793
130	P297	239.44814	35.97409	-0.193	1.605
131	P298	239.70594	36.01584	1.054	3.743
132	P300	239.72302	36.30443	-0.455	-0.299
133	P301	239.25695	36.80629	-1.257	1.204
134	P302	239.38143	36.63473	-3.418	-2.853
135	P305	239.80324	37.35221	-1.703	1.915
136	P306	239.35554	37.79517	-2.521	2.551
137	P309	239.04876	38.08999	-2.578	-0.292
138	P512	240.30555	37.56264	-2.448	0.663
139	P513	239.34983	34.90726	-0.002	0.599
140	P514	239.59025	35.01071	0.552	0.954
141	P515	239.76015	34.87055	-0.567	1.780
142	P516	239.61661	35.10620	0.012	0.439
143	P518	239.92469	35.02003	0.235	1.481
144	P519	240.20756	34.50781	0.951	0.976
145	P520	240.38360	34.63048	1.62	-0.096
146	P521	240.18465	34.88857	1.631	0.599
147	P522	240.46394	35.08661	1.117	2.733
148	P523	239.13973	35.30445	0.229	1.271
149	P525	239.19186	35.42577	-0.212	1.070
150	P527	239.39525	35.75414	-0.615	-2.232
151	P528	239.45455	35.32781	-0.073	1.859
152	P529	239.64617	35.44045	0.187	2.083
153	P530	239.51957	35.62480	-1.039	-0.428
154	P531	239.46340	35.79269	-0.386	2.564
155	P532	239.73297	35.63381	0.46	2.960
156	P533	239.62905	35.74793	0.068	2.222
157	P534	237.76239	37.06123	-1.111	-0.647
158	P535	239.89858	35.23513	0.367	2.022
159	P536	239.97498	35.27977	0.222	2.397
160	P537	240.06466	35.31680	0.811	3.285
161	P538	239.88750	35.53417	0.731	3.384
162	P539	239.81795	35.70267	0.477	3.476

163	P540	239.86936	35.80128	-0.355	2.300
164	P541	239.99932	35.68673	0.29	3.507
165	P542	239.70740	35.68891	0.174	2.561
166	P543	240.28678	35.31899	0.803	4.062
167	P546	239.84512	35.92790	0.857	3.586
168	P547	240.09064	35.93470	-0.737	1.700
169	P548	240.49606	34.46681	0.128	0.174
170	P550	240.88538	34.66008	1.26	2.264
171	P551	240.84543	34.85620	2.37	1.860
172	P552	239.75504	35.68672	0.316	3.006
173	P553	241.12103	34.83509	1.228	2.754
174	P554	241.15197	34.79230	0.395	1.242
175	P555	241.33058	34.69499	0.814	1.101
176	P556	241.45455	34.77111	-0.676	-1.439
177	P557	241.34441	34.94438	1.116	1.653
178	P558	241.38835	35.13861	-0.083	1.760
179	P562	241.81126	34.98213	-0.925	0.491
180	P567	241.24642	35.42095	1.72	3.539
181	P568	241.87349	35.25431	-0.991	0.093
182	P569	241.87623	35.37797	-0.657	0.395
183	P570	241.73996	35.66735	0.369	1.258
184	P571	241.23329	36.23137	-0.238	3.512
185	P572	241.04540	36.58552	-0.934	2.891
186	P573	241.73950	36.09309	-0.012	1.291
187	P576	239.03000	35.66966	1.699	0.581
188	P578	239.76097	35.69433	0.096	2.916
189	P579	241.99424	35.03876	-1.095	-0.120
190	P591	241.98353	35.15242	-1.088	-0.553
191	P602	239.77211	35.72916	0.717	2.916
192	P616	242.10667	35.42456	-0.562	0.147
193	P725	240.25439	37.08890	-0.851	2.912
194	P782	239.78381	35.69382	-0.324	4.803
195	P787	238.41917	36.79948	-1.456	0.681
196	P788	238.52124	36.74433	-3.127	0.511
197	P789	239.52827	35.94659	-0.207	2.473
198	P790	239.48462	35.92915	1.611	2.005
199	P808	241.37855	34.83602	NO RATE	0.357
200	P811	241.98339	35.15243	NO RATE	0.521
201	P812	241.98346	35.15250	NO RATE	0.128
202	PBHR	238.72759	35.70895	NO RATE	-0.456
203	PKDB	239.45845	35.94524	-1.265	1.594
204	QCY2	238.86265	36.16107	-0.192	1.179
205	RAMT	242.31665	35.33871	-1.946	-0.165

206	RCA2	240.28000	34.49998	0.197	1.525
207	RNCH	239.47517	35.89999	0.243	1.773
208	ROCP	237.93705	37.81642	NO RATE	-0.575
209	RSTP	241.80708	34.87508	-0.944	0.071
210	RSVY	240.81557	34.54148	0.676	1.885
211	S300	238.44173	37.66651	-0.751	0.373
212	SAOB	238.55282	36.76530	-0.057	0.286
213	SCCP	237.99793	37.65184	NO RATE	-0.712
214	SHP5	239.32872	35.26863	NO RATE	5.932
215	SLAC	237.79574	37.41652	0.222	-0.789
216	SOMT	240.93567	34.31994	-1.428	-0.371
217	SRES	239.04283	35.81842	3.543	3.120
218	SRS1	239.93478	34.00434	-0.721	-0.997
219	TBLP	239.63966	35.91741	-0.242	5.107
220	TEHA	241.53021	35.14306	NO RATE	4.401
221	THAC	241.64720	35.03269	NO RATE	1.585
222	THCP	241.58543	35.15818	-0.024	1.419
223	UCSB	240.15619	34.41330	-1.678	1.763
224	USLO	239.33891	35.31180	-1.185	0.536
225	VAN5	239.43649	34.82661	0.669	-0.405
226	VCST	240.51614	34.85150	-1.113	0.247
227	VNDP	239.38355	34.55631	0.195	0.153
228	WGPP	241.01631	35.01085	-2.601	-0.836
229	WIN2	237.85937	37.65265	-0.591	-0.584
230	WKPK	241.25848	34.56850	0.947	2.004
231	WLHL	238.99585	35.97258	NO RATE	0.685
232	ZOA2	237.98411	37.54303	-0.348	-0.396

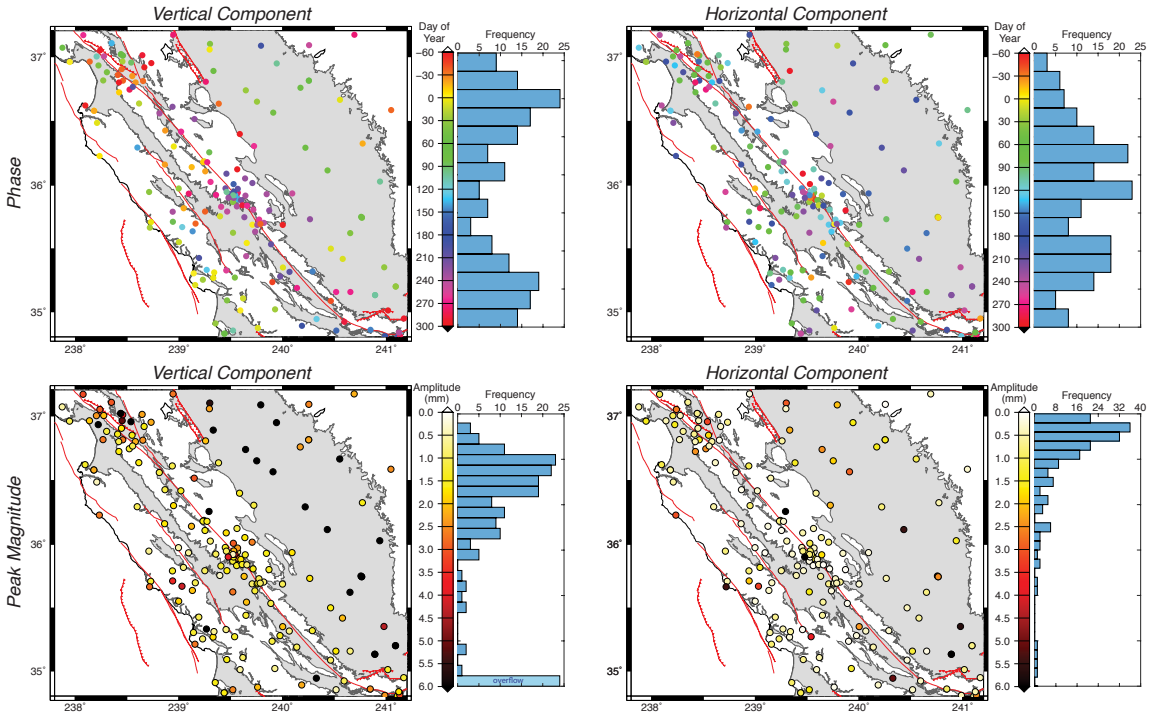

Figure A1 Phase and associated peak magnitudes for GPS stations processed in the NA12 reference frame, colored according to the scale to the right of the map. The histogram to the right of the scale summarizes the distribution of plotted values for each map. Boundary for figures is denoted as a gray dotted line in Figure 1. Faults are drawn in red and basins from the California Department of Water Resources are shaded in gray.

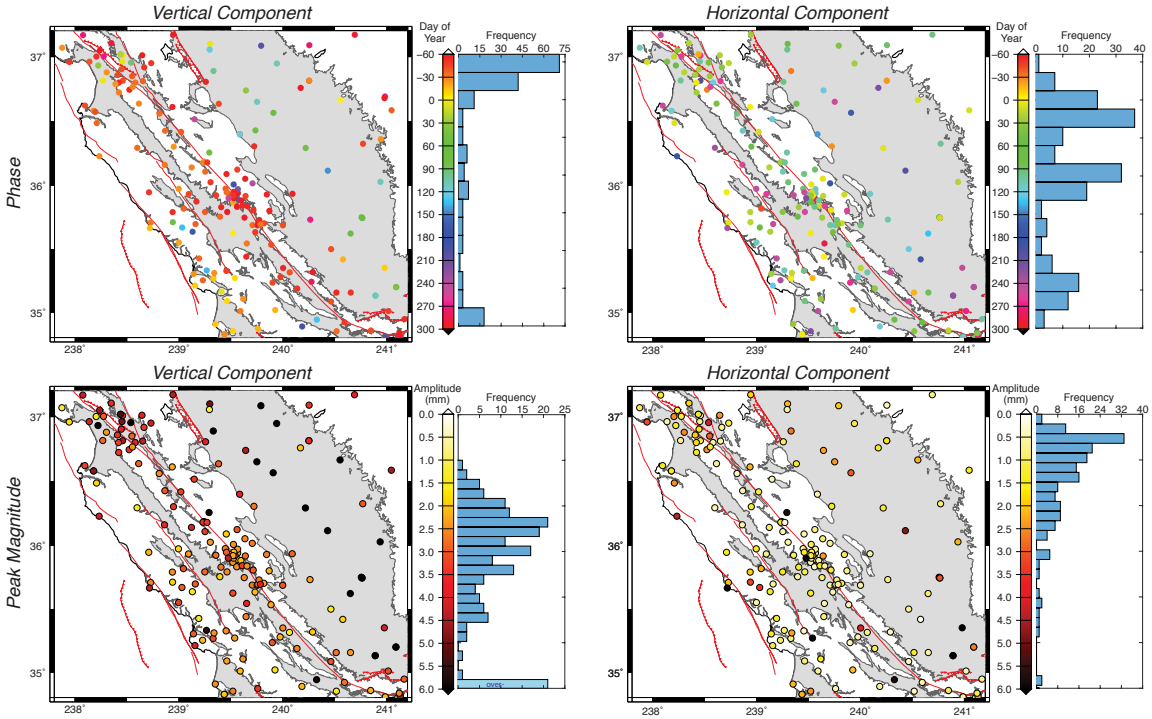

Figure A2 Same as Figure A1, but for GPS stations in the IGS08 reference frame.

Figure A3a

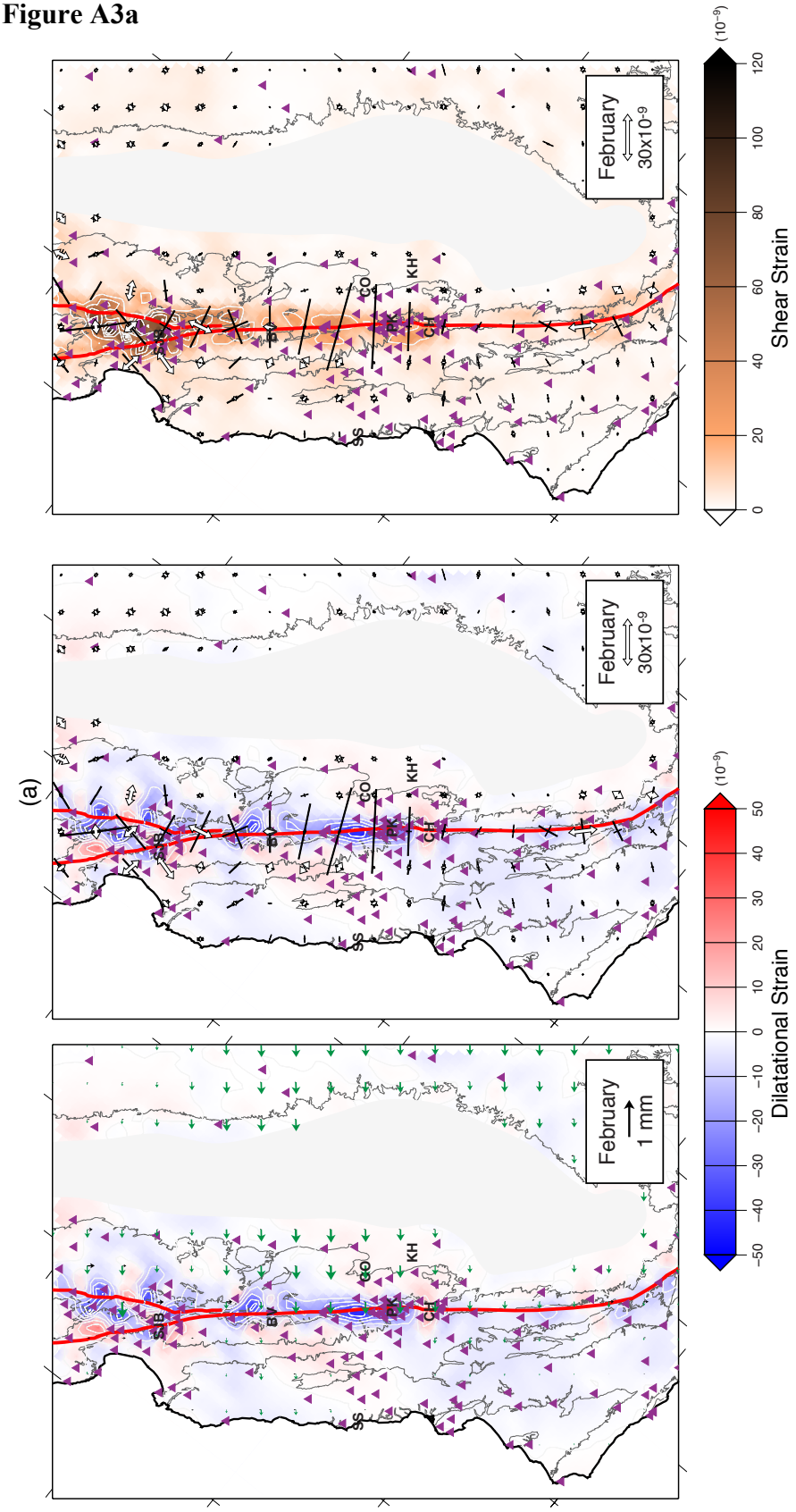
(a)
February
30x10⁻⁹
February
30x10⁻⁹
February
1 mm
Shear Strain
Dilatational Strain
(10⁻⁹)
0
20
40
60
80
100
120
50
40
30
20
10
0
−10
−20
−30
−40
−50
SS
CH
PK
CO
KH
BA
SB

Figure A3b

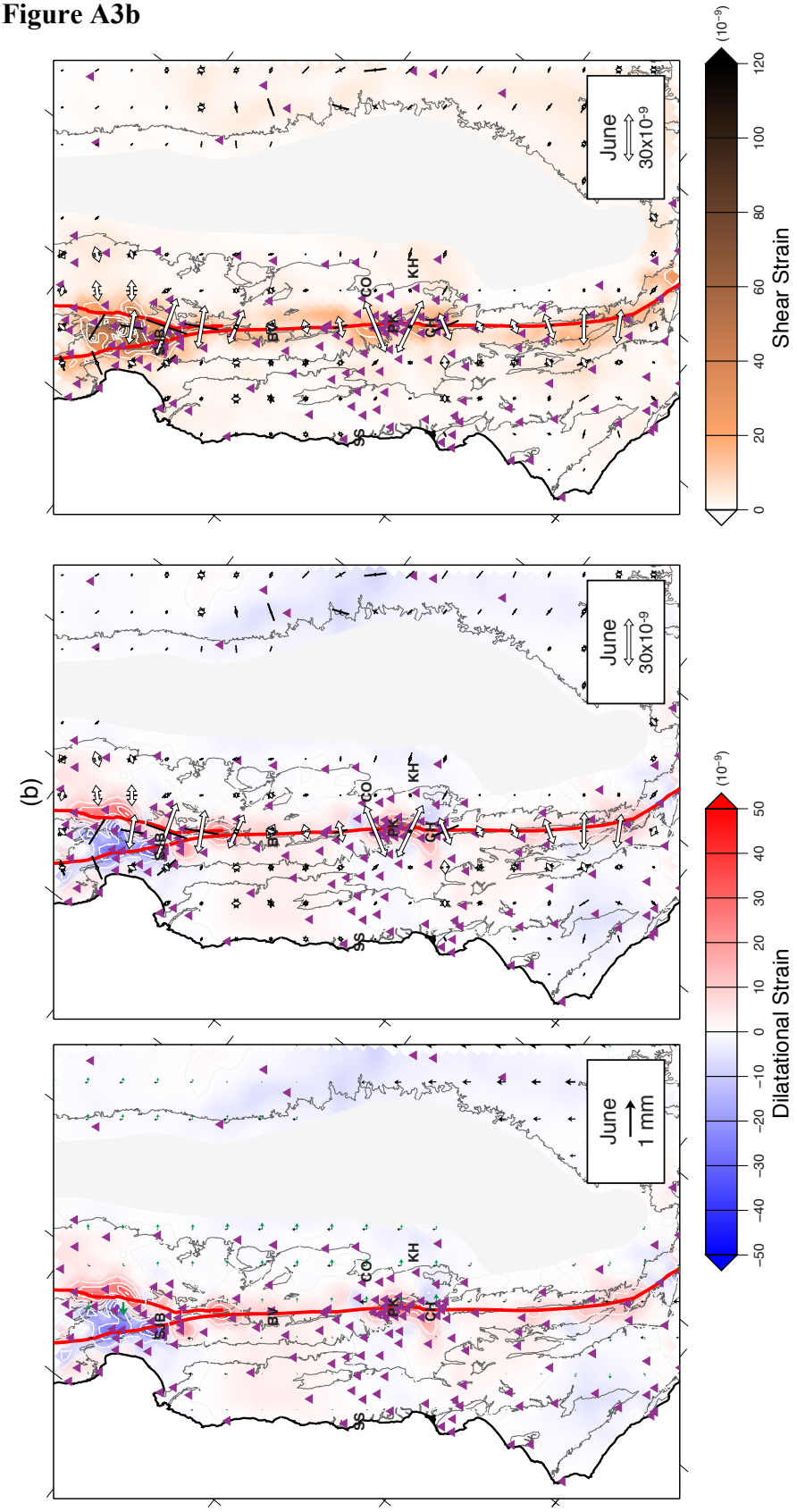
(b)
June
30x10⁻⁹
June
30x10⁻⁹
June
1 mm
Shear Strain
Dilatational Strain
(10⁻⁹)
(10⁻⁹)
0
20
40
60
80
100
120
50
40
30
20
10
0
−10
−20
−30
−40
−50
SJB
BK
CO
KH
PK
GF
SS

Figure A3c

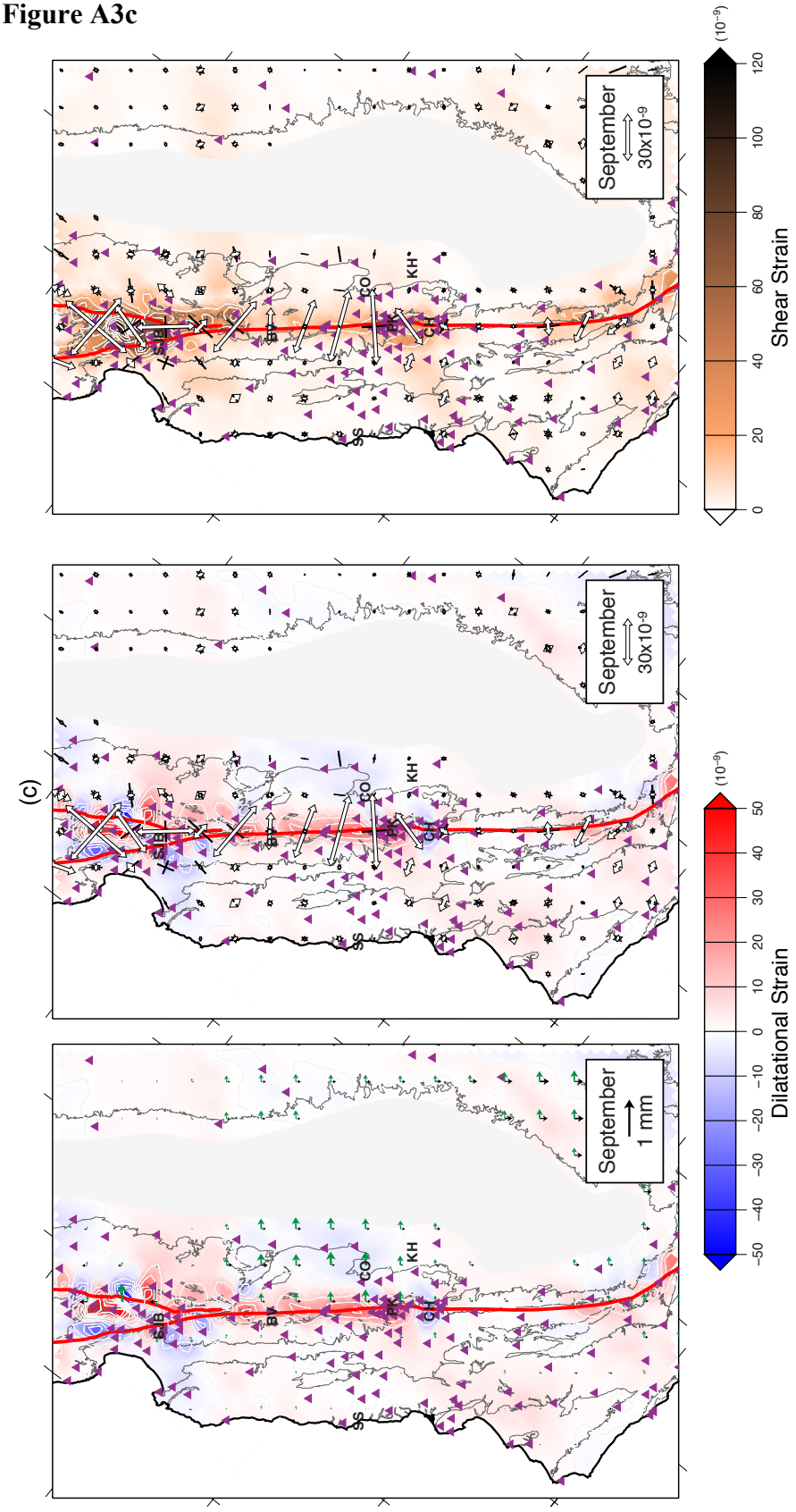
(c)
September
30x10⁻⁹
September
30x10⁻⁹
September
1 mm
SB
BK
CO
KH
CH
SS
Shear Strain
Dilatational Strain
(10⁻⁹)
0
20
40
60
80
100
120
50
40
30
20
10
0
−10
−20
−30
−40
−50

Figure A3 (Three previous pages) Models of dilatation (left and middle panels) and shear (right panel) strain for **(a)** February, **(b)** June, and **(c)** September. The far-left panel of each month (a – c) shows modeled displacements in a Pacific reference frame, which have been decomposed into fault normal (green vectors) and fault parallel (black vectors) motion. This is the model using on-fault and off-fault standard deviations of 750 and 1.5, respectively (a weak fault). The middle and right panels display the principle strain axes, using the convention of black as maximum contraction and white as maximum extensional. The region where input gridded filtered displacements were eliminated from the solution due to lack of data (gray-shaded region) has been covered over by a white polygon. Locations San Juan Battista (SJB), San Simeon (SS), Bitterwater Valley (BV), Parkfield (PK), Cholame (CH), Coalinga (CO) and Kettleman Hills (KH) are denoted. Faults are drawn in red, stations used to create the input gridded displacements are drawn as purple triangles, and basins (from CA Department of Water Resources) are outlined in gray.

Figure A4a

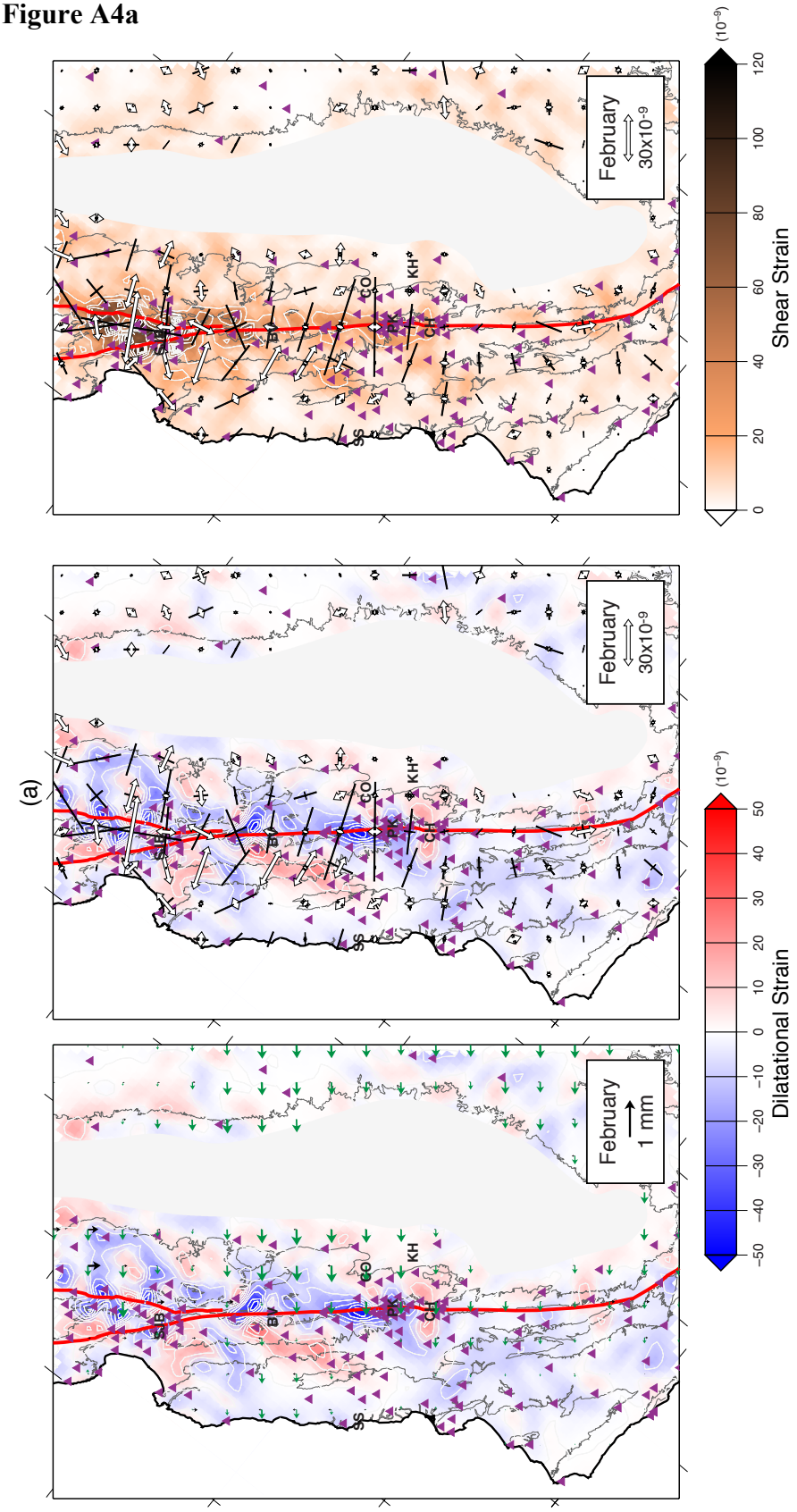
(a)
February
30x10⁻⁹
February
30x10⁻⁹
February
1 mm
Shear Strain
Dilatational Strain
(10⁻⁹)
0
20
40
60
80
100
120
−50
−40
−30
−20
−10
0
10
20
30
40
50
SS
PK
CH
BA
CO
KH

Figure A4b

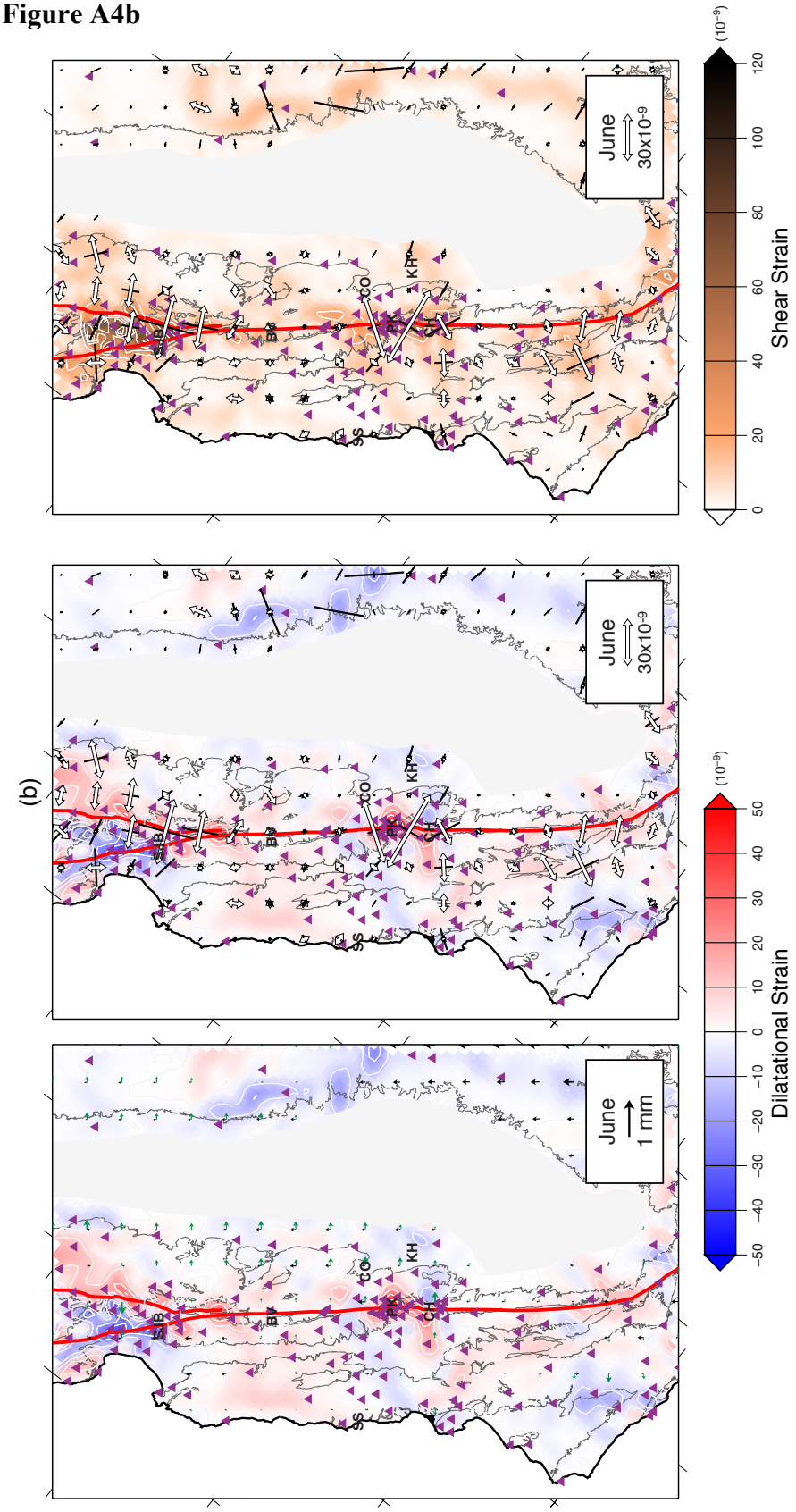
(b)
June
30x10⁻⁹
June
30x10⁻⁹
June
1 mm
Shear Strain
Dilatational Strain
(10⁻⁹)
SB
BK
CO
KH
CH
SS

Figure A4c

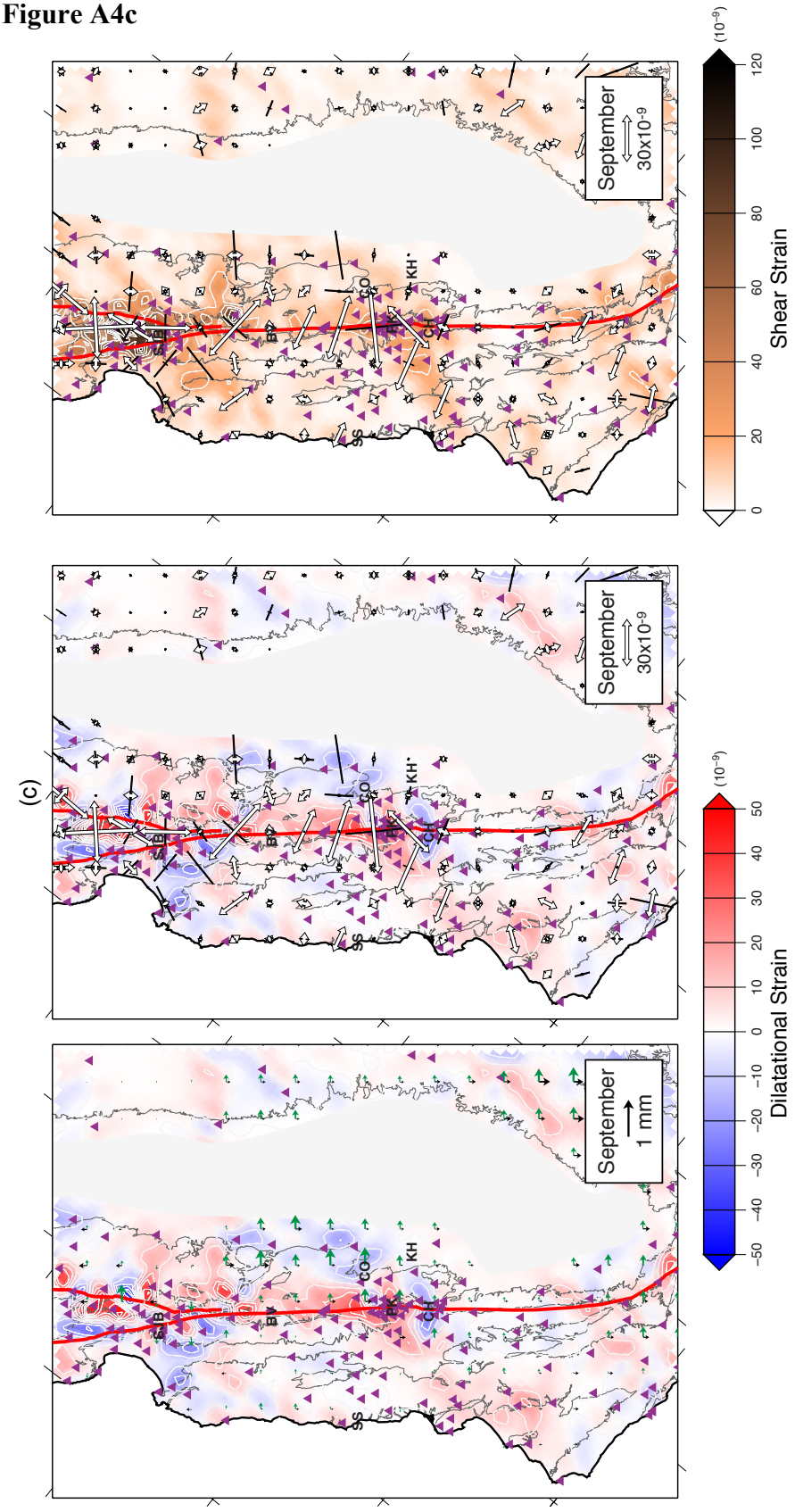
(c)
September
30x10⁻⁹
Shear Strain
(10⁻⁹)
0
20
40
60
80
100
120
September
30x10⁻⁹
Dilatational Strain
(10⁻⁹)
50
40
30
20
10
0
−10
−20
−30
−40
−50
September
1 mm
SB
BP
CO
KH
PK
CH
SS

Figure A4 (Three previous pages) Models of dilatation (left and middle panels) and shear (right panel) strain for **(a)** February, **(b)** June, and **(c)** September. The far-left panel of each month (a – c) shows modeled displacements in a Pacific reference frame, which have been decomposed into fault normal (green vectors) and fault parallel (black vectors) motion. This is the model using on-fault and off-fault standard deviations of 2000 and 4.0, respectively (a strong fault). The middle and right panels display the principle strain axes, using the convention of black as maximum contraction and white as maximum extensional. The region where input gridded filtered displacements were eliminated from the solution due to lack of data (gray-shaded region) has been covered over by a white polygon. Locations San Juan Battista (SJB), San Simeon (SS), Bitterwater Valley (BV), Parkfield (PK), Cholame (CH), Coalinga (CO) and Kettleman Hills (KH) are denoted. Faults are drawn in red, stations used to create the input gridded displacements are drawn as purple triangles, and basins (from CA Department of Water Resources) are outlined in gray.

Figure A5a

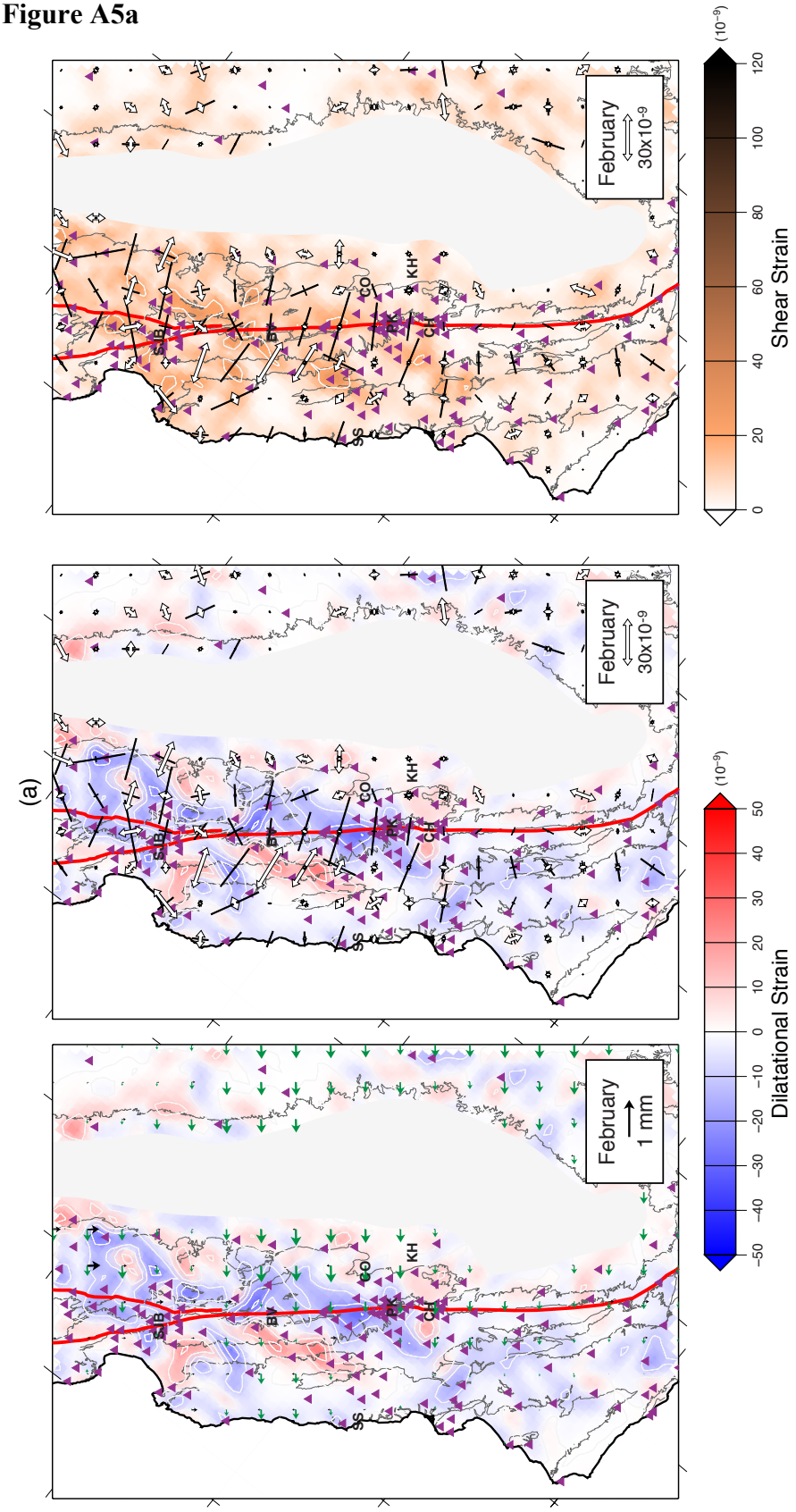
(a)
February
30x10⁻⁹
February
30x10⁻⁹
February
1 mm
Shear Strain
Dilatational Strain
(10⁻⁹)
0
20
40
60
80
100
120
50
40
30
20
10
0
−10
−20
−30
−40
−50
KH
CO
BK
CH
SS

Figure A5b

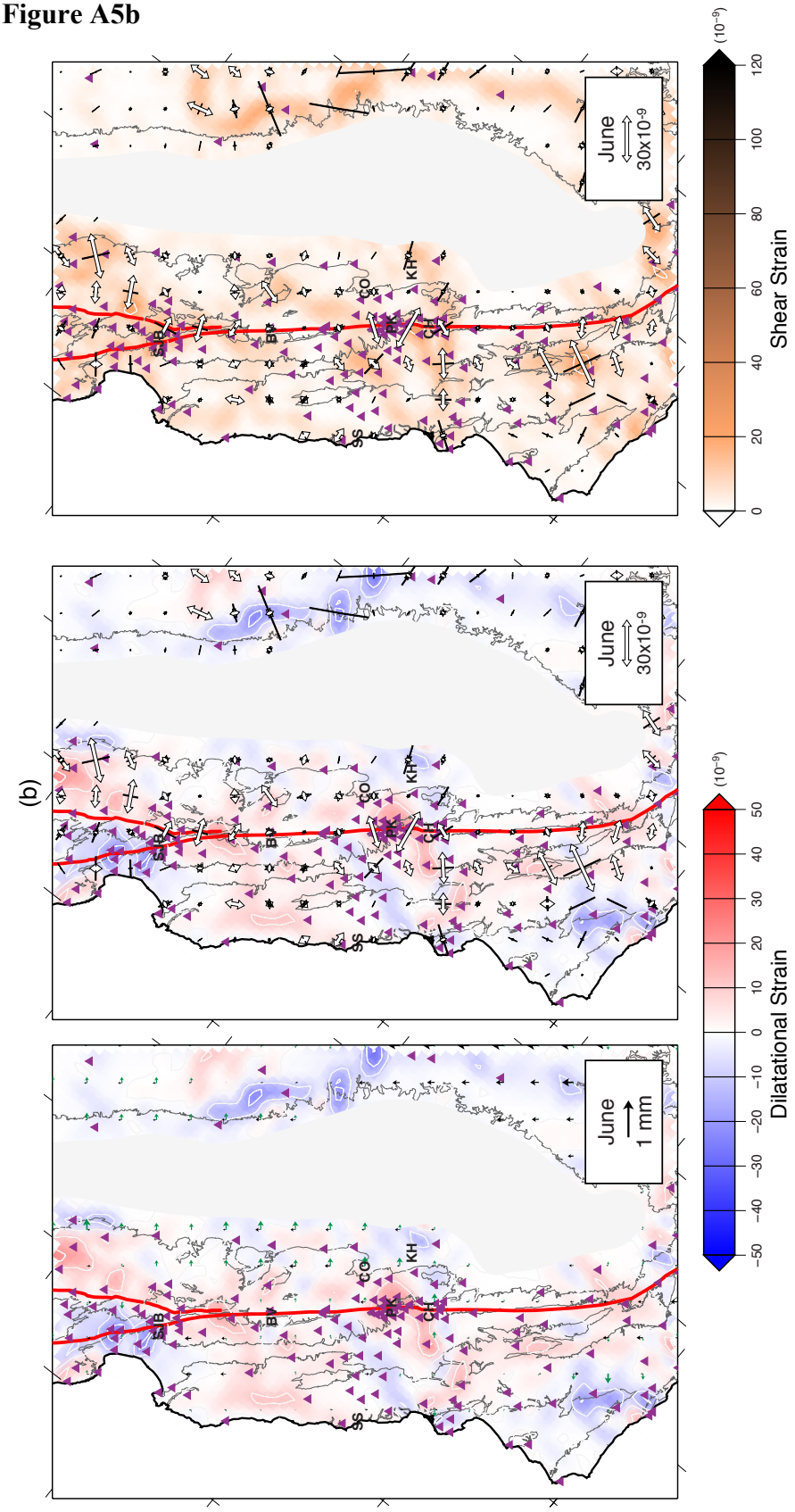
(b)
June
30x10⁻⁹
June
30x10⁻⁹
June
1 mm
Shear Strain
Dilatational Strain
(10⁻⁹)
(10⁻⁹)
0
20
40
60
80
100
120
50
40
30
20
10
0
−10
−20
−30
−40
−50
SS
CH
BK
CO
KH
BB
EB

Figure A5c

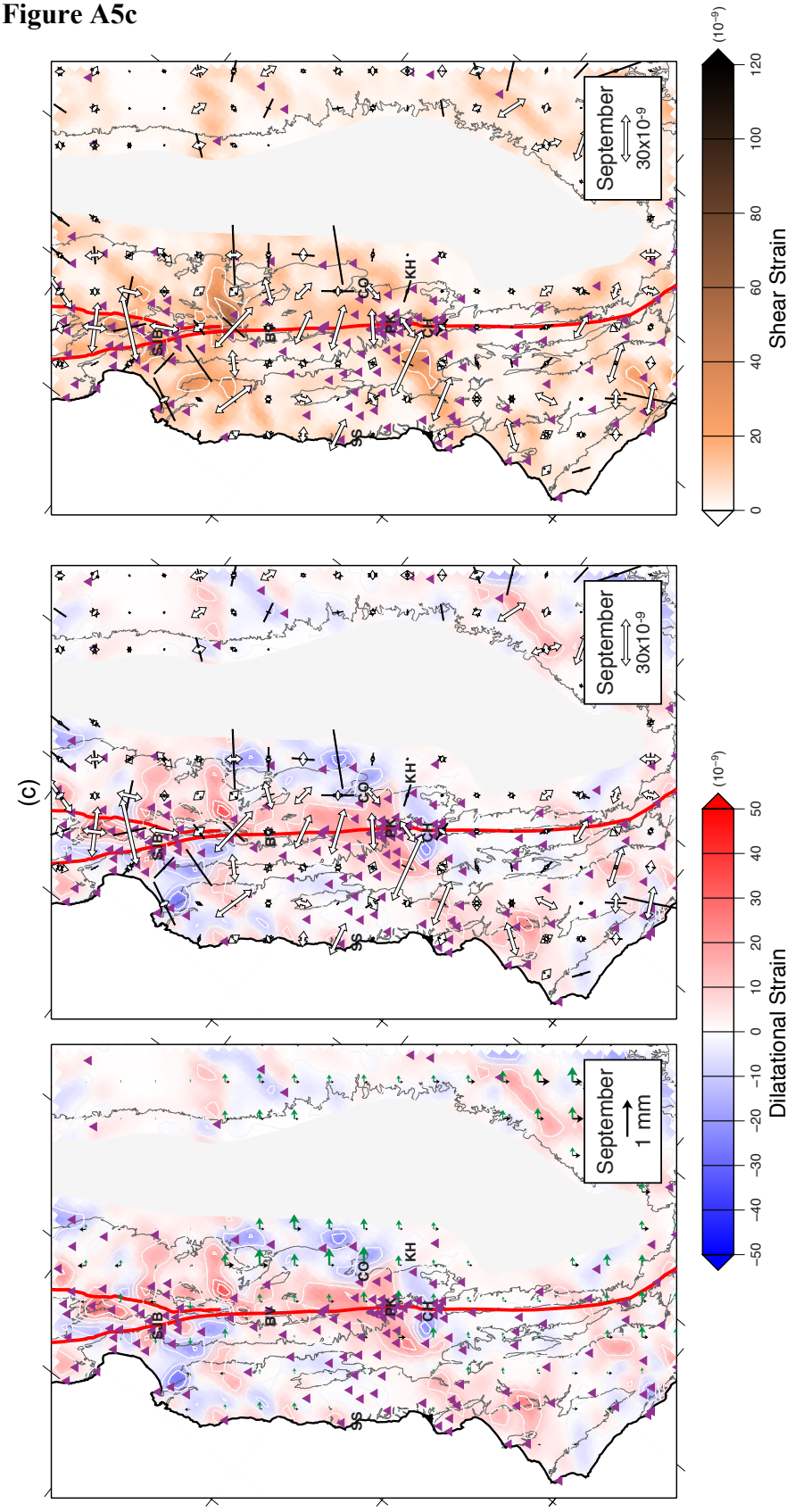
September
30x10⁻⁹
Shear Strain
(10⁻⁹)
0
20
40
60
80
100
120
September
30x10⁻⁹
Dilatational Strain
(10⁻⁹)
50
40
30
20
10
0
−10
−20
−30
−40
−50
September
1 mm
(c)
SB
SB
CO
KH
PK
CH
SS

Figure A5 (Three previous pages) Models of dilatation (left and middle panels) and shear (right panel) strain for **(a)** February, **(b)** June, and **(c)** September. This is the homogeneous model, which only considers filtered seasonal gridded displacements as input since no fault information is provided. The far-left panel of each month (a – c) shows modeled displacements in a Pacific reference frame, which have been decomposed into fault normal (green vectors) and fault parallel (black vectors) motion. The middle and right panels display the principle strain axes, using the convention of black as maximum contraction and white as maximum extensional. The region where input gridded filtered displacements were eliminated from the solution due to lack of data (gray-shaded region) has been covered over by a white polygon. Locations San Juan Battista (SJB), San Simeon (SS), Bitterwater Valley (BV), Parkfield (PK), Cholame (CH), Coalinga (CO) and Kettleman Hills (KH) are denoted. Faults are drawn in red, stations used to create the input gridded displacements are drawn as purple triangles, and basins (from CA Department of Water Resources) are outlined in gray.